J. Mech. Phys. Solids 154 (2021) 104514

Contents lists available at ScienceDirect

Journal of the Mechanics and Physics of Solids

journal homepage: www.elsevier.com/locate/jmps

The remarkable bending properties of perforated plates

Bhavesh Shrimali [a], Matteo Pezzulla [b], Samuel Poincloux [b], Pedro M. Reis [b], Oscar Lopez-Pamies [a,*]

[a] Department of Civil and Environmental Engineering, University of Illinois at Urbana-Champaign, IL, 61801, United States of America
[b] Flexible Structures Laboratory, École polytechnique Fédérale de Lausanne, Route Cantonale, 1015 Lausanne, Switzerland

ARTICLE INFO

Keywords:
Dimension reduction
Homogenization
Kirchhoff–Love plate
Microstructures

ABSTRACT

Motivated by recent experiments on the bending of porous strips towed through a fluid bath, a combined theoretical and experimental study is made of the bending response of perforated plates. The focus is on the practically relevant class of thin plates (with thickness $\mathtt{h}$) made of a homogeneous isotropic material that is perforated with periodic distributions (with unit-cell size ε) of monodisperse holes spanning a large range of porosities, from the dilute limit to nearly the percolation threshold. From the theoretical point of view, with the objective of quantifying the roles that the various constitutive and geometric inputs play on the their bending response, the perforated plates are modeled by means of three different approaches: (*i*) as 3D structures made of a perforated nonlinear elastic material and as 2D structures made of homogeneous linear elastic materials whose effective properties result from (*ii*) first taking the limit of dimension reduction ($\mathtt{h} \searrow 0$) and then that of homogenization ($\varepsilon \searrow 0$) and, vice versa, (*iii*) first taking the limit of homogenization ($\varepsilon \searrow 0$) and then that of dimension reduction ($\mathtt{h} \searrow 0$). From the experimental point of view, laser-engraved molds are utilized to fabricate perforated elastomeric plates with hexagonal distributions of elliptical holes. The resulting perforated plates are then subject to cantilever-bending due to their self weight and their pointwise deformation measured by means of X-ray tomography. Remarkably, counter to the general expectation from available mathematical results for heterogeneous plates at large, the results indicate that the bending response of perforated plates is fairly insensitive to whether the holes are smaller or larger than the plate thickness. Instead, it is dominated by their porosity, while the spatial distribution and shape of the underlying holes only have relatively marginal effects.

1. Introduction

The use of thin perforated plates for functional and/or artistic purposes dates back millennia. Throughout such a rich history, driven by recurrent advances in manufacturing capabilities, there have been repeated surges in their experimental and theoretical study. Of late, advances in manufacturing processes such as 3D printing and laser cutting have provided the means of fabricating heterogeneous – not just perforated – plates with complex microstructures at unprecedented ease and spatial resolution. For example, Guttag et al. (2018) fabricated porous polymeric strips via laser cutting and measured their bending stiffnesses experimentally to investigate their deformation due to fluid loading at high-Reynolds-number conditions. As part of a more recent investigation on fluid–structure interactions, making use of micro-fabrication techniques, Pezzulla et al. (2020) fabricated thin perforated plates of about 150 mm^2 area with a thickness of $\mathtt{h} = 0.4$ mm and a hexagonal distribution of monodisperse circular holes of radii ranging

* Corresponding author.
E-mail addresses: bshrima2@illinois.edu (B. Shrimali), matt@eng.au.dk (M. Pezzulla), samuel.poincloux@epfl.ch (S. Poincloux), pedro.reis@epfl.ch (P.M. Reis), pamies@illinois.edu (O. Lopez-Pamies).

https://doi.org/10.1016/j.jmps.2021.104514
Received 9 April 2021; Received in revised form 25 May 2021; Accepted 26 May 2021
Available online 2 June 2021

from 50 μm to 5 mm at $f = 0.5$ porosity. Counter to the general expectation, the cantilever-bending response of their plates was found to be largely insensitive to the size of the holes, irrespectively of whether these were smaller or larger than the plate thickness. It was this unforeseen observation that prompted the combined theoretical and experimental study that we present in this paper.

From a theoretical point of view, among the slew of existing formulations aimed at characterizing the mechanical behavior of plates, the Kirchhoff–Love plate theory (Love, 1888) is the simplest one that can accurately describe the response of thin plates; see, e.g., the classical account by Timoshenko and Woinowsky-Krieger (1959). Ciarlet and Destuynder (1979) derived the governing equations of a Kirchhoff–Love plate as a limiting case of a 3D linear elastic *homogeneous* continuum where one of its dimensions – its thickness $\mathtt{h}$ – goes to 0. Their dimension-reduction procedure paved the way for subsequent systematic studies of *heterogeneous* plates; see the historical review contained in the book by Sab and Lebée (2015), for instance. We mention in particular the seminal contributions of Caillerie (1984) and Kohn and Vogelius (1984) who worked out the governing equations for the mechanical response of periodically heterogeneous plates in the limits of infinitesimally small plate thickness as $\mathtt{h} \searrow 0$ and unit-cell size as $\varepsilon \searrow 0$ from a 3D linear elastic periodically heterogeneous continuum. Their results showed that the governing equations are of Kirchhoff–Love-plate type wherein the effective bending stiffness tensor is homogeneous but given by *different formulae* – defined implicitly in terms of solutions of partial differential equations (PDEs) over different types of unit cells – depending on how fast the small parameters $\mathtt{h}$ and ε go to 0 with respect to one another and on the specifics of the microstructures being considered. In other words, as one might expect intuitively, their results established that the bending response of heterogeneous plates is, in principle, strongly dependent on the size of their thicknesses relative to that of their heterogeneities, as well as on the details of the latter.

As is well known, the governing equations of Kirchhoff–Love plates do not generally admit closed-form solutions and thus must be solved numerically, especially when they are heterogeneous; see, e.g., the monograph by Reddy (2007) for a fairly complete list of the handful of available analytical solutions. Most numerical efforts have focused on the finite element (FE) method. Early schemes based on conforming C^1-continuous FEs (Argyris et al., 1968; Bell, 1969), or analogous non-conforming FEs (Morley, 1968), are rarely used in practice because of the intricacies of their implementation. A relatively more popular approach has been to consider the governing equations of Mindlin plates from the outset as an approximation of the Kirchhoff–Love equations in the limit of small plate thickness and to employ standard C^0-continuous FEs to solve those. However, such an approach is inconsistent when dealing with boundary-value problems that involve free boundaries; see, e.g., Destuynder and Nevers (1988). More recently, Veiga et al. (2007) have introduced a new method that allows solving the Kirchhoff–Love equations for any type of boundary conditions with standard C^0-continuous FEs.

We presume that it is likely because of the lack of experimental impetus, together with the computational challenges of the methods preceding that of Veiga et al. (2007) for plates with free boundaries, that a thorough investigation of the mechanical response of thin perforated plates in particular, and heterogeneous plates in general, has not been put forth in the literature.

In this context, the object of this paper is to study the macroscopic bending properties of a wide range of thin perforated plates directly in terms of their thicknesses and microstructures, both theoretically and experimentally. Our focus is on the practically relevant class of plates made of a homogeneous isotropic material that is perforated with square and hexagonal distributions of elliptical and rectangular monodisperse holes spanning a broad spectrum of porosities, ranging from the dilute limit to nearly the percolation threshold.

The organization of the paper is as follows. We begin in Section 2 by describing the geometry and microstructures of the plates under investigation. We proceed in Section 3 by presenting the three different theoretical approaches that we employ to describe their bending response. Specifically, in Section 3.1, we present a model that views the plates as 3D heterogeneous structures made of a perforated nonlinear elastic material, whereas in Sections 3.2 and 3.3 we view them through a more idealized lens as 2D structures made of homogeneous linear elastic materials whose effective properties result from first taking the limit of dimension reduction $\mathtt{h} \searrow 0$ and then that of homogenization $\varepsilon \searrow 0$ and, vice versa, first taking the limit of homogenization $\varepsilon \searrow 0$ and then that of dimension reduction $\mathtt{h} \searrow 0$. Making use of the three formulations presented in Section 3, Sections 4, 5, and 6 are devoted, respectively, to the analyses of the convergence from 3D to the 2D plate theories as $\mathtt{h} \searrow 0$ and $\varepsilon \searrow 0$, the sensitivities of the response of the plates to the order in which the dimension-reduction and homogenization limits are taken, and to the porosity, spatial distribution, and shape of the holes. Section 7 details the experimental component of this work, including the fabrication process of the plates and the measurements obtained from X-ray tomography of their cantilever-bending response due to their self weight. Section 8 is then devoted to confronting the theoretical and experimental results. We close by recording a few concluding remarks in Section 9.

2. Geometry of the plates and their perforated microstructures

For definiteness, we consider rectangular plates of lengths $\mathtt{l}_1$ and $\mathtt{l}_2 = O(\mathtt{l}_1)$ in the $\mathbf{e}_1$ and $\mathbf{e}_2$ directions and constant thickness $\mathtt{h} \ll \mathtt{l}_1, \mathtt{l}_2$ in the $\mathbf{e}_3$ direction; see Figs. 1 and 2. Here, $\{\mathbf{e}_i\}$ stands for the laboratory frame of reference. We place its origin at the plates' midplane along a corner so that, in their undeformed and stress-free configurations, the plates occupy the domain

$$\mathcal{P}^{\mathtt{h}} = \left\{ \mathbf{X} : (X_1, X_2) \in \Omega,\ |X_3| < \pm\frac{\mathtt{h}}{2} \right\}, \tag{1}$$

where

$$\Omega = \left\{ \mathbf{x} : 0 < x_\alpha < \mathtt{l}_\alpha \right\} \tag{2}$$

denotes the region occupied by the plates' midplane and where, for later convenience, we have made use of the notation

$$x_\alpha = X_\alpha.$$

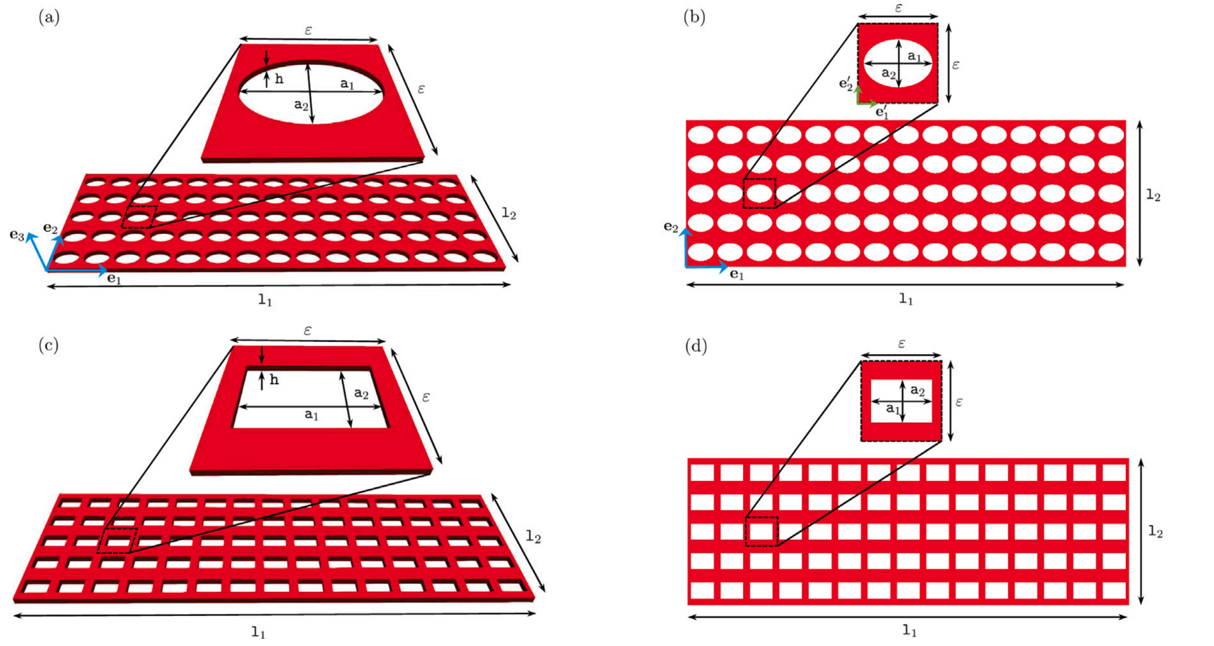

Fig. 1. Schematic of the plates with dimensions $l_1 \times l_2 \times h$ and *square distributions* of (a)–(b) *elliptical* and (c)–(d) *rectangular holes* with aspect ratio $\omega = a_2/a_1$. Parts (a) and (c) show the plates from a 3D perspective, while parts (b) and (d) show their midplanes. The defining unit cells with dimensions $\varepsilon \times \varepsilon \times h$ and $\varepsilon \times \varepsilon$ are also shown for both perspectives.

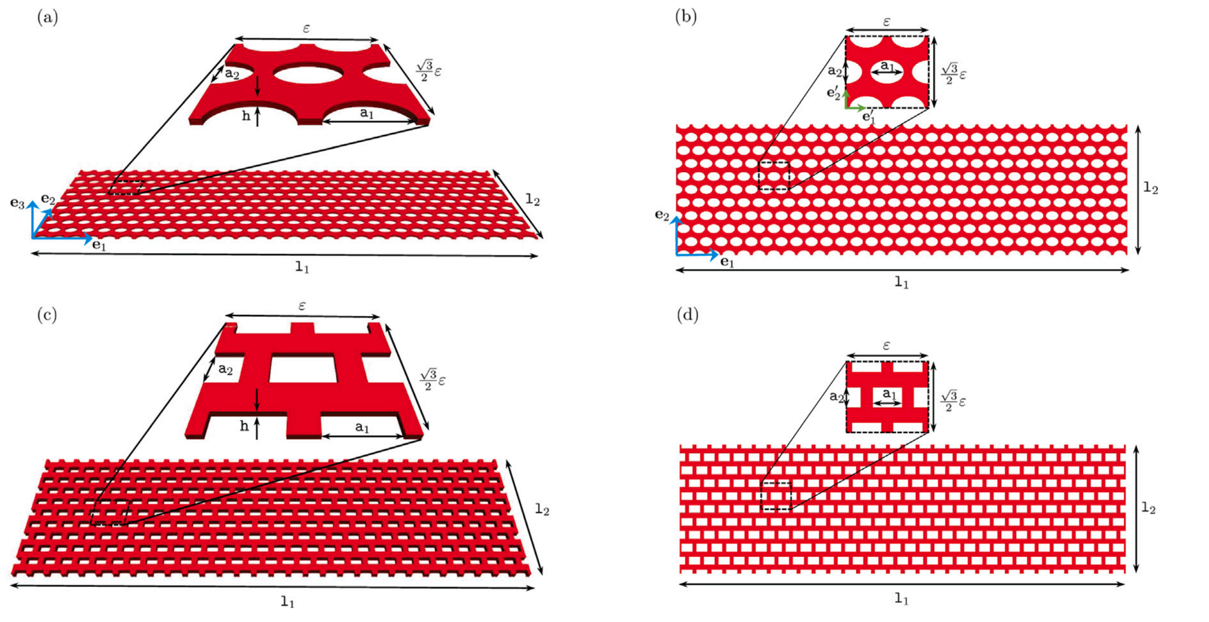

Fig. 2. Schematic of the plates with dimensions $l_1 \times l_2 \times h$ and *hexagonal distributions* of (a)–(b) *elliptical* and (c)–(d) *rectangular holes* with aspect ratio $\omega = a_2/a_1$. Parts (a) and (c) show the plates from a 3D perspective, while parts (b) and (d) show their midplanes. The defining unit cells with dimensions $\varepsilon \times \sqrt{3}/2\varepsilon \times h$ and $\varepsilon \times \sqrt{3}/2\varepsilon$ are also shown for both perspectives.

Throughout, Latin indices range from 1 to 3, Greek ones range from 1 to 2, and, unless otherwise stated, the summation convention applies whenever indices are repeated. Moreover, we denote by $\mathbf{N}$ the unit outward normal to the boundary of the plate $\partial\mathcal{P}^{h}$, and by $\mathbf{n}$ and $\boldsymbol{\tau}$ the unit outward normal and the unit counterclockwise tangent to the boundary of the plates' midplane $\partial\Omega$, respectively.

As representative cases, the experiments and simulations presented below in Sections 4 through 8 pertain to plates of lengths $l_1 = 40$ mm, $l_2 = 40$ mm, and thicknesses $h = \{0.73, 0.80, 2.00\}$ mm. They will be subject to cantilever-bending due to their self weight and, thus, part of their boundary will be clamped ($\mathcal{C}$), while the complementary part will be free ($\mathcal{F}$). For later reference,

Table 1
The 12 classes of perforated microstructures considered in this study and the critical value $f^{\star}$ of the porosity f at which they percolate.

Plate	Hole spatial distribution	Hole shape	$f^{\star}$
SE0.9	square	ellipse ($\omega = 0.9$)	0.707
SE1.0	square	circle	0.785
SE1.2	square	ellipse ($\omega = 1.2$)	0.654
SR0.9	square	rectangle ($\omega = 0.9$)	0.900
SR1.0	square	square	1.000
SR1.2	square	rectangle ($\omega = 1.2$)	0.833
HE0.9	hexagonal	ellipse ($\omega = 0.9$)	0.816
HE1.0	hexagonal	circle	0.907
HE1.2	hexagonal	ellipse ($\omega = 1.2$)	0.839
HR0.9	hexagonal	rectangle ($\omega = 0.9$)	0.962
HR1.0	hexagonal	square	0.866
HR1.2	hexagonal	rectangle ($\omega = 1.2$)	0.722

we shall denote those boundaries as

$$\partial\mathcal{P}^{\mathtt{h}}_{C} = \left\{\mathbf{X} : (X_1, X_2) \in \partial\Omega_C,\ |X_3| \leq \pm\frac{\mathtt{h}}{2}\right\} \qquad \text{and} \qquad \partial\mathcal{P}^{\mathtt{h}}_{\mathcal{F}} = \partial\mathcal{P}^{\mathtt{h}} \setminus \partial\mathcal{P}^{\mathtt{h}}_{C}$$

with

$$\partial\Omega_C = \left\{\mathbf{x} :\ x_1 = 0,\ 0 \leq x_2 \leq \mathtt{l}_2\right\} \qquad \text{and} \qquad \partial\Omega_{\mathcal{F}} = \partial\Omega \setminus \partial\Omega_C,$$

and the set of corner points in $\partial\Omega_{\mathcal{F}}$ as

$$\mathcal{V} = \{\mathbf{x} :\ (x_1, x_2) = (\mathtt{l}_1, 0),\ (\mathtt{l}_1, \mathtt{l}_2)\}.$$

Our interest is in heterogeneous plates made of a homogeneous isotropic matrix material perforated periodically with square (S) and hexagonal (H) distributions of elliptical (E) and rectangular (R) holes that are aligned with the principal directions $\mathbf{e}'_1$ and $\mathbf{e}'_2$ of the unit cells, feature three different aspect ratios $\omega = \mathtt{a}_2/\mathtt{a}_1 = 0.9, 1.0, 1.2$, and span the broad spectrum of porosities $f \in [0, 0.60]$. In all, we consider 12 different classes of perforated microstructures. Figs. 1 and 2 provide schematics of these classes and illustrate their defining geometric quantities.

For later reference, Table 1 labels each one of the 12 classes of plates that are investigated in this paper and identifies their corresponding percolation thresholds $f^{\star}$.

Remark 1. For clarity of presentation, as tacitly assumed in the description of the undeformed configuration (1)–(2), we model the holes in the plates *not* as boundaries of the domain but, rather, as a second-phase material of vanishingly small stiffness. In other words, we view the perforated plates as composite plates made of two different materials.

3. Three theoretical descriptions of the bending response of the plates

With the objective of identifying the extents to which the various constitutive and geometric quantities influence their bending response, we model the plates described above via three different approaches:

i The first approach, laid out in Section 3.1, consists in describing the 3D finite-size geometry of the plates precisely as given and in idealizing the behavior of their matrix material as isotropic nonlinear elastic. In other words, the plates are viewed as 3D structures made of a perforated homogeneous isotropic material capable of undergoing nonlinear elastic deformations.

ii The second approach, outlined in Section 3.2, consists in considering that the strains at all points in the plates remain within the linear elastic regime of the matrix material and, furthermore, in idealizing both their small thickness $\mathtt{h}$ and the period ε of their repeating unit cell to be infinitesimally small, ordered such that $\mathtt{h} \ll \varepsilon$. The plates are thus viewed as 2D structures, resulting from the dimension-reduction limit $\mathtt{h} \searrow 0$, that are made of a homogeneous linear elastic material whose effective properties results from the homogenization limit $\varepsilon \searrow 0$.

iii As finally described in Section 3.3, the third approach consists in also considering that the strains at all points in the plates remain within the linear elastic regime of the matrix material and in taking $\mathtt{h}$ and ε to be infinitesimally small, but ordered such that $\varepsilon \ll \mathtt{h}$. Thus, in this approach the plates are also viewed as 2D structures made of a homogeneous linear elastic material. The difference with respect to the approach in Section 3.2 is that the size of the heterogeneity ε of the plates is taken to be much smaller than their thickness $\mathtt{h}$, as opposed to the other way around.

3.1. The plates viewed as 3D structures made of a perforated nonlinear elastic material

Kinematics. Material points in the plates are identified by their initial position vector $\mathbf{X} \in \mathcal{P}^{\mathtt{h}}$. Due to externally applied stimuli to be described below, the position vector $\mathbf{X}$ of a material point moves to a new position specified by $\mathbf{x} = \mathbf{X} + \mathbf{u}(\mathbf{X})$ in terms of the displacement field $\mathbf{u}(\mathbf{X})$. We write the deformation gradient at $\mathbf{X}$ as $\mathbf{F}(\mathbf{X}) = \mathbf{I} + \mathrm{Grad}\,\mathbf{u}(\mathbf{X})$.

Constitutive behavior. The constitutive behavior of the plates is taken to be nonlinear elastic, in particular, hyperelastic. We write its stored-energy function as

$$W^{\varepsilon}(\mathbf{X},\mathbf{F})=\chi(\varepsilon^{-1}\mathbf{x})W(\mathbf{F}), \tag{3}$$

where $W(\mathbf{F})$ denotes the stored-energy function describing the elastic response of the matrix material and $\chi(\varepsilon^{-1}\mathbf{x})$ stands for its periodic characteristic function, that is, $\chi=1$ if $\mathbf{X}$ is outside a hole and zero otherwise. Note that for the plates with square distributions of holes $\chi(\varepsilon^{-1}\mathbf{x})=\chi((\varepsilon^{-1}x_1+z_1)\mathbf{e}'_1+(\varepsilon^{-1}x_2+z_2)\mathbf{e}'_2)$, while for those with hexagonal distributions of holes $\chi(\varepsilon^{-1}\mathbf{x})=\chi((\varepsilon^{-1}x_1+z_1)\mathbf{e}'_1+(\varepsilon^{-1}x_2+\sqrt{3}/2z_2)\mathbf{e}'_2)$, where z_1 and z_2 are integers; see Figs. 1 and 2.

For later use, we recall here that basic physical requirements dictate that $W(\mathbf{QF})=W(\mathbf{F})$ for all proper orthogonal tensors $\mathbf{Q}$ and that the initial modulus of elasticity of the plates, defined by

$$L^{\varepsilon}_{ijkl}(\mathbf{X})=\chi(\varepsilon^{-1}\mathbf{x})L_{ijkl}:=\frac{1}{2}\frac{\partial^2W^{\varepsilon}}{\partial F_{ij}F_{kl}}(\mathbf{X},\mathbf{I})=\frac{1}{2}\chi(\varepsilon^{-1}\mathbf{x})\frac{\partial^2W}{\partial F_{ij}F_{kl}}(\mathbf{I}), \tag{4}$$

satisfies, in turn, the symmetry and positive-definite conditions

$$L_{ijkl}=L_{klij}=L_{jikl}=L_{ijlk},\qquad L_{ijkl}\Xi_{ij}\Xi_{kl}\geq\theta\Xi_{pq}\Xi_{pq}\ \forall\boldsymbol{\Xi}\in\mathbb{R}^3\times\mathbb{R}^3, \tag{5}$$

where θ is some positive constant.

In the simulations presented below in Sections 4 and 8, we will employ the isotropic Neo-Hookean stored-energy function

$$W(\mathbf{F})=\frac{\mu}{2}\left[\mathbf{F}\cdot\mathbf{F}-3\right]-\mu\ln(\det\mathbf{F})+\frac{\Lambda}{2}(\det\mathbf{F}-1)^2 \tag{6}$$

with

$$\mu=0.45\,\text{MPa}\qquad\text{and}\qquad\Lambda=5.12\,\text{MPa} \tag{7}$$

to characterize the elastic response of the elastomer VPS (vinyl polysiloxane) used for the matrix material in the experiments (see Section 7). Its initial modulus of elasticity is simply given by

$$L_{ijkl}=\mu(\delta_{ik}\delta_{jl}+\delta_{il}\delta_{jk})+\Lambda\delta_{ij}\delta_{kl}, \tag{8}$$

from which one can readily deduce that the material constants μ and Λ in (6) are the Lamé constants. The values (7) correspond then to a material with Young's modulus $E=\mu(2\mu+3\Lambda)/(\mu+\Lambda)=1.3$ MPa and Poisson's ratio $\nu=\Lambda/2(\mu+\Lambda)=0.46$.

Boundary conditions and body force. Consistent with the cantilever-bending experiments outlined in Section 7, we shall consider a combination of free and clamped boundary conditions on the plates. Moreover, the plates will be subject to their self weight and thus to the body force (per unit reference volume)

$$B^{\varepsilon}_{\alpha}(\mathbf{X})=0,\quad B^{\varepsilon}_3(\mathbf{X})=B_3(\varepsilon^{-1}\mathbf{x})=-\chi(\varepsilon^{-1}\mathbf{x})\rho g, \tag{9}$$

where ρ denotes the density of the matrix material and g stands for the acceleration of gravity. In all the simulations presented below, we make use of the value $\rho=1148$ kg/m^3 for the density of the elastomer VPS. Moreover, the acceleration of gravity will be taken as $g=1.27$ m/s^2 to account for the fact that the experiments are carried out with the plates entirely submerged in water (see Section 7).

Governing equations. Absent inertia, in view of the above-outlined kinematics, constitutive behavior, boundary conditions, and body force, the mechanical response of the plates is governed by the boundary-value problem

$$\begin{cases}\dfrac{\partial}{\partial X_j}\left[\dfrac{\partial W^{\varepsilon}}{\partial F_{ij}}\left(\mathbf{X},\mathbf{F}^{\mathrm{h}\varepsilon}(\mathbf{X})\right)\right]+B^{\varepsilon}_i(\mathbf{X})=0,\quad \mathbf{X}\in\mathcal{P}^{\mathrm{h}}\\ u^{\mathrm{h}\varepsilon}_i(\mathbf{X})=0,\quad \mathbf{X}\in\partial\mathcal{P}^{\mathrm{h}}_{C}\\ \left[\dfrac{\partial W^{\varepsilon}}{\partial F_{ij}}\left(\mathbf{X},\mathbf{F}^{\mathrm{h}\varepsilon}(\mathbf{X})\right)\right]N_j(\mathbf{X})=0,\quad \mathbf{X}\in\partial\mathcal{P}^{\mathrm{h}}_{\mathcal{F}}\end{cases} \tag{10}$$

for the displacement field $\mathbf{u}^{\mathrm{h}\varepsilon}(\mathbf{X})$, where we have made use of the notation $\mathbf{F}^{\mathrm{h}\varepsilon}(\mathbf{X})=\mathbf{I}+\mathrm{Grad}\,\mathbf{u}^{\mathrm{h}\varepsilon}(\mathbf{X})$. Eq. (10) is nothing more than balance of linear momentum in the absence of inertia, specialized to the constitutive behavior (3). Balance of angular momentum is automatically satisfied by virtue of the assumed material frame indifference of the stored-energy function $W(\mathbf{F})$.

Remark 2. The boundary-value problem (10) is a standard finite elastostatics problem. It is thus straightforward to solve it numerically with the FE method. All the solutions for (10) that we present in this paper are based on linear simplicial elements and on a Newton-like nonlinear method together with a direct solver for the resulting linear system of equations at each Newton iteration. We remark that linear simplicial elements are sufficient in the present context thanks to the fact that the first-Lamé-constant-to-shear-modulus ratio is only about $\Lambda/\mu=11$ and hence not exceedingly large to cause volumetric locking.

3.2. The plates viewed as 2D structures made of a homogeneous linear elastic material: the case of $\mathtt{h} \ll \varepsilon$

For the case of plates where the thickness $\mathtt{h}$ and unit-cell size ε are much smaller than the other two plate dimensions $\mathtt{l}_1$ and $\mathtt{l}_2$, it is sensible to take the limits $\mathtt{h} \searrow 0$ and $\varepsilon \searrow 0$ in (10) in order to simplify the calculations involved and, by the same token, to gain more precise insight into their mechanical response. Not surprisingly, as already recalled in the Introduction, it turns out that how fast the parameters $\mathtt{h}$ and ε go to 0 with respect to one another has a significant impact on the resulting limit.

In this subsection, we consider the extreme case when $\mathtt{h} \searrow 0$ first and then $\varepsilon \searrow 0$. In other words, we consider the case of plates whose thicknesses are much smaller than their heterogeneities, that is, $\mathtt{h} \ll \varepsilon$. Caillerie (1984) showed rigorously in Section 4 of his work that in such a limit, assuming that the strains remain within the linear elastic regime of the matrix material, the displacement field defined by the boundary-value problem (10) reduces to

$$\mathbf{u}^{\mathtt{h}\varepsilon}(\mathbf{X}) = (0, 0, w(\mathbf{x}))$$

to leading order. Physically, the function $w(\mathbf{x})$ stands for the displacement of the midplane of the plate in the $\mathbf{e}_3$ direction (i.e., the deflection). It is defined implicitly as the solution of the boundary-value problem

$$\begin{cases} \dfrac{\partial^2}{\partial x_\alpha \partial x_\beta}\left[\widehat{M}_{\alpha\beta\gamma\delta}\dfrac{\partial^2 w}{\partial x_\gamma \partial x_\delta}(\mathbf{x})\right] = \widehat{B}, \quad \mathbf{x} \in \Omega \\ \begin{cases} w(\mathbf{x}) = 0 \\ n_\alpha(\mathbf{x})\dfrac{\partial w}{\partial x_\alpha}(\mathbf{x}) = 0 \end{cases}, \quad \mathbf{x} \in \partial\Omega_C \\ \begin{cases} n_\alpha(\mathbf{x})n_\beta(\mathbf{x})\widehat{M}_{\alpha\beta\gamma\delta}\dfrac{\partial^2 w}{\partial x_\gamma \partial x_\delta}(\mathbf{x}) = 0 \\ n_\beta(\mathbf{x})\dfrac{\partial}{\partial x_\alpha}\left[\widehat{M}_{\alpha\beta\gamma\delta}\dfrac{\partial^2 w}{\partial x_\gamma \partial x_\delta}(\mathbf{x})\right] + \tau_\nu(\mathbf{x})\dfrac{\partial}{\partial x_\nu}\left[n_\alpha(\mathbf{x})\tau_\beta(\mathbf{x})\widehat{M}_{\alpha\beta\gamma\delta}\dfrac{\partial^2 w}{\partial x_\gamma \partial x_\delta}(\mathbf{x})\right] = 0 \end{cases}, \quad \mathbf{x} \in \partial\Omega_{\mathcal{F}} \\ \left[\!\left[n_\alpha(\mathbf{x})\tau_\beta(\mathbf{x})\widehat{M}_{\alpha\beta\gamma\delta}\dfrac{\partial^2 w}{\partial x_\gamma \partial x_\delta}(\mathbf{x}) \right]\!\right] = 0, \quad \mathbf{x} \in \mathcal{V} \end{cases}, \tag{11}$$

where we recall that Ω denotes the domain occupied by the midplane of the plate, while $\partial\Omega_C$, $\partial\Omega_{\mathcal{F}}$, and $\mathcal{V}$ stand for the parts of the boundary $\partial\Omega$ that are clamped, free, and for the corner points in $\partial\Omega_{\mathcal{F}}$. The components of the fourth-order tensor $\widehat{\mathbf{M}}$ in (11) are given by the formula

$$\widehat{M}_{\alpha\beta\gamma\delta} = \frac{1}{|Y|}\int_Y \chi(\mathbf{y})M_{\alpha\beta\mu\nu}\left(\delta_{\mu\gamma}\delta_{\nu\delta} + \frac{\partial^2 \varpi_{\gamma\delta}}{\partial y_\mu \partial y_\nu}(\mathbf{y})\right)\mathrm{d}\mathbf{y} \tag{12}$$

in terms of the unit cell Y defining the microstructure – here, $Y = [0,1] \times [0,1]$ for the square distributions of holes and $Y = [0,1] \times [0, \sqrt{3}/2]$ for the hexagonal distributions – of the plate, the characteristic function $\chi(\mathbf{y})$ of its matrix material, and associated bending stiffness tensor

$$M_{\alpha\beta\gamma\delta} = \frac{\mathtt{h}^3}{12}\left(L_{\alpha\beta\gamma\delta} - \frac{L_{\alpha\beta 33}L_{\gamma\delta 33}}{L_{3333}}\right), \tag{13}$$

where $\varpi_{\gamma\delta}(\mathbf{y})$ is the Y-periodic function defined as the unique solution of the 2D unit-cell boundary-value problem

$$\begin{cases} \dfrac{\partial^2}{\partial y_\alpha \partial y_\beta}\left[\chi(\mathbf{y})M_{\alpha\beta\gamma\delta}\dfrac{\partial^2 \varpi_{\mu\nu}}{\partial y_\gamma \partial y_\delta}(\mathbf{y})\right] = -\dfrac{\partial^2 \chi}{\partial y_\alpha \partial y_\beta}(\mathbf{y})M_{\alpha\beta\mu\nu}, \quad \mathbf{y} \in Y \\ \int_Y \varpi_{\mu\nu}(\mathbf{y})\mathrm{d}\mathbf{y} = 0 \end{cases}, \tag{14}$$

and where

$$\widehat{B} = -\frac{1}{|Y|}\int_Y \chi(\mathbf{y})\rho g \mathrm{d}\mathbf{y} = -(1-f)\rho g. \tag{15}$$

Eqs. (11) are nothing more than the governing equations for a Kirchhoff–Love plate with homogeneous – albeit possibly anisotropic – bending stiffness tensor $\widehat{\mathbf{M}}$ that is clamped at $\partial\Omega_C$, free at $\partial\Omega_{\mathcal{F}}$, and that is subjected to the body force $\widehat{B}$. The following remarks are in order.

Remark 3 (*The Effective Bending Stiffness Tensor* $\widehat{\mathbf{M}}$.). The effective bending stiffness tensor (12) that emerges in the dimension-reduced and homogenized equation (11) is independent of the choice of the domain Ω occupied by the midplane of the plate, the boundary conditions on $\partial\Omega$, and the presence of the body force (9). Moreover, it follows from the symmetries $(5)_1$ of the local modulus of elasticity (4) and the definition (14) of the function $\varpi_{\mu\nu}(\mathbf{y})$ that $\widehat{\mathbf{M}}$ satisfies the standard symmetry properties

$$\widehat{M}_{\alpha\beta\gamma\delta} = \widehat{M}_{\gamma\delta\alpha\beta} = \widehat{M}_{\beta\alpha\gamma\delta} = \widehat{M}_{\alpha\beta\delta\gamma}$$

of the bending stiffness tensor of a standard homogeneous plate; see, e.g., Duvaut and Metellus (1976).

Evaluation of the formula (12) for $\widehat{\mathbf{M}}$ requires knowledge of the Y-periodic function $\varpi_{\mu\nu}(\mathbf{y})$ defined by the PDE (14), which is in essence the governing equation for a Kirchhoff–Love plate with a piecewise constant bending stiffness tensor over a periodic domain. Accordingly, its numerical solution is amenable to the FE approach of Veiga et al. (2007) suitably modified to account for the periodicity constraint. All the solutions for (14) that we present in this paper are based on that approach and make use of simplicial elements, with quadratic approximations for the displacement field and linear approximations for the rotations, and a direct solver for the resulting linear system of equations (Shrimali and Lopez-Pamies, 2021).

Remark 4 (*The Effective Body Force* $\widehat{B}$.)**.** The effective body force (15) that emerges in the dimension-reduced and homogenized equation (11) is simply the arithmetic average of the local body force (9). Accordingly, its evaluation merely requires knowledge of the porosity f in the given plate.

Remark 5 (*Numerical Solution*)**.** Being a standard boundary-value problem for a Kirchhoff–Love plate, the Eqs. (11) can be readily solved numerically with the FE approach of Veiga et al. (2007). All the solutions for (11) that we present in this paper are based on that approach.

3.3. The plates viewed as 2D structures made of a homogeneous linear elastic material: the case of $\varepsilon \ll \mathtt{h}$

In this subsection, we consider the successive limits of dimension reduction and homogenization in an inverse order of that presented in the previous subsection. Physically, this corresponds to the opposite extreme case of plates whose heterogeneities are much smaller than their thicknesses, that is, $\varepsilon \ll \mathtt{h}$.

Thus, in the limit when first the length scale of the microstructure $\varepsilon \searrow 0$ and then the thickness of the plate $\mathtt{h} \searrow 0$, assuming still that the strains remain within the linear elastic regime of the matrix material, the displacement field defined by the boundary-value problem (10) can be shown to reduce to (Caillerie, 1984; Section 5)

$$\mathbf{u}^{\mathtt{h}\varepsilon}(\mathbf{X}) = (0, 0, w(\mathbf{x}))$$

to leading order. Here, the displacement $w(\mathbf{x})$ of the midplane of the plate in the $\mathbf{e}_3$ direction is defined implicitly as the solution of the boundary-value problem

$$\begin{cases} \dfrac{\partial^2}{\partial x_\alpha \partial x_\beta}\left[\widetilde{M}_{\alpha\beta\gamma\delta}\dfrac{\partial^2 w}{\partial x_\gamma \partial x_\delta}(\mathbf{x})\right] = \widetilde{B}, \quad \mathbf{x} \in \Omega \\ \begin{cases} w(\mathbf{x}) = 0 \\ n_\alpha(\mathbf{x})\dfrac{\partial w}{\partial x_\alpha}(\mathbf{x}) = 0 \end{cases}, \quad \mathbf{x} \in \partial\Omega_{\mathcal{C}} \\ \begin{cases} n_\alpha(\mathbf{x}) n_\beta(\mathbf{x})\widetilde{M}_{\alpha\beta\gamma\delta}\dfrac{\partial^2 w}{\partial x_\gamma \partial x_\delta}(\mathbf{x}) = 0 \\ n_\beta(\mathbf{x})\dfrac{\partial}{\partial x_\alpha}\left[\widetilde{M}_{\alpha\beta\gamma\delta}\dfrac{\partial^2 w}{\partial x_\gamma \partial x_\delta}(\mathbf{x})\right] + \tau_\nu(\mathbf{x})\dfrac{\partial}{\partial x_\nu}\left[n_\alpha(\mathbf{x})\tau_\beta(\mathbf{x})\widetilde{M}_{\alpha\beta\gamma\delta}\dfrac{\partial^2 w}{\partial x_\gamma \partial x_\delta}(\mathbf{x})\right] = 0 \end{cases}, \quad \mathbf{x} \in \partial\Omega_{\mathcal{F}} \\ \left[\!\left[n_\alpha(\mathbf{x})\tau_\beta(\mathbf{x})\widetilde{M}_{\alpha\beta\gamma\delta}\dfrac{\partial^2 w}{\partial x_\gamma \partial x_\delta}(\mathbf{x}) \right]\!\right] = 0, \quad \mathbf{x} \in \mathcal{V} \end{cases}, \tag{16}$$

where the components of the effective bending stiffness tensor $\widetilde{\mathbf{M}}$ are given by the formula

$$\widetilde{M}_{\alpha\beta\gamma\delta} = \frac{\mathtt{h}^3}{12}\left(\widetilde{L}_{\alpha\beta\gamma\delta} - \frac{\widetilde{L}_{\alpha\beta 33}\widetilde{L}_{\gamma\delta 33}}{\widetilde{L}_{3333}}\right) \tag{17}$$

in terms of the unit cell $\mathcal{Y}$ defining the microstructure – here, $\mathcal{Y} = [0,1] \times [0,1] \times [0,1]$ for the square distributions of holes and $\mathcal{Y} = [0,1] \times [0, \sqrt{3}/2] \times [0,1]$ for the hexagonal distributions – of the plate and of its homogenized modulus of elasticity

$$\widetilde{L}_{ijkl} = \frac{1}{|\mathcal{Y}|}\int_{\mathcal{Y}} \chi(\mathbf{y}) L_{ijpq}\left(\delta_{pk}\delta_{ql} + \frac{\partial \varpi_{pkl}}{\partial y_q}(\mathbf{y})\right) \mathrm{d}\mathbf{y}, \tag{18}$$

where $\varpi_{pkl}(\mathbf{y})$ is the $\mathcal{Y}$-periodic function defined as the unique solution of the 3D unit-cell boundary-value

$$\begin{cases} \dfrac{\partial}{\partial y_j}\left[\chi(\mathbf{y}) L_{ijkl}\dfrac{\partial \varpi_{kpq}}{\partial y_l}(\mathbf{y})\right] = -\dfrac{\partial \chi}{\partial y_j}(\mathbf{y}) L_{ijpq}, \quad \mathbf{y} \in \mathcal{Y} \\ \int_{\mathcal{Y}} \varpi_{kpq}(\mathbf{y})\mathrm{d}\mathbf{y} = 0 \end{cases}, \tag{19}$$

and where

$$\widetilde{B} = \widehat{B} = -(1-f)\rho g. \tag{20}$$

Similar to (11), Eqs. (16) are the governing equations of a Kirchhoff–Love plate featuring a homogeneous but possibly anisotropic bending stiffness tensor $\widetilde{\mathbf{M}}$ that is clamped at $\partial\Omega_{\mathcal{C}}$, free at $\partial\Omega_{\mathcal{F}}$, and that is subjected to the body force $\widetilde{B}$.

Remark 6 (*The Effective Bending Stiffness Tensor* $\widetilde{\mathbf{M}}$.). Much like the effective bending stiffness tensor (12) in (11), the effective bending stiffness tensor (17) that emerges in the homogenized and dimension-reduced equation (16) is independent of the choice of the domain Ω occupied by the midplane of the plate, the boundary conditions on $\partial\Omega$, and the presence of the body force (9). Moreover, the symmetries $(5)_1$ of the local modulus of elasticity (4) together with the definition (19) of the function $\varpi_{kpq}(\mathbf{y})$ imply the standard symmetries

$$\widetilde{M}_{\alpha\beta\gamma\delta} = \widetilde{M}_{\gamma\delta\alpha\beta} = \widetilde{M}_{\beta\alpha\gamma\delta} = \widetilde{M}_{\alpha\beta\delta\gamma}.$$

Evaluation of the formula (17) for $\widetilde{\mathbf{M}}$ requires knowledge of the $\mathcal{Y}$-periodic function $\varpi_{kpq}(\mathbf{y})$ defined by the PDE (19), which is in essence a linear elastostatics problem with a piecewise constant modulus of elasticity over a periodic domain. Its numerical solution is hence amenable to a standard FE approach; see, e.g., the Appendix in Spinelli et al. (2015). The FE solutions for (19) that we present in this paper make use of linear simplicial elements and a direct solver for the resulting linear system of equations.

Remark 7 (*The Effective Body Force* $\widetilde{B}$.). The effective body force (20) that emerges in the homogenized and dimension-reduced equation (16) is identical to the one that emerges in (11), namely, it is the arithmetic average of the local body force (9).

Remark 8 (*Numerical Solution*). All the solutions for (16) that we present in this paper are based on the FE approach due to Veiga et al. (2007) and, much like for (11), make use of linear simplicial elements (again, with quadratic approximations for the displacement field and linear approximations for the rotations) and a direct solver for the resulting linear system of equations.

4. Convergence from 3D to the 2D plate theories as $\mathtt{h} \searrow 0$ and $\varepsilon \searrow 0$

The thickness $\mathtt{h}$ and unit-cell size ε of actual thin perforated plates, however small they might be, are invariably of *finite* value. A question of paramount practical relevance is then how small $\mathtt{h}$ and ε need to be with respect to the macroscopic dimensions of the plate at hand (here, $\mathtt{l}_1$ and $\mathtt{l}_2$) and with respect to each other for the 2D asymptotic formulations (11) and (16) to be applicable, in the sense that they deliver practically the same solution as the 3D formulation (10). Our aim here is not to provide a detailed answer to this question in the spirit of those available in the literature for homogeneous isotropic plates (Arnold et al., 2002), but, rather, to provide a simple (albeit not rigorous) rule of thumb for use in practice.

To that end, and also to prepare the stage for the comparisons with experiments that follow, we confront the solutions generated by the 3D approach (10) to those generated by the 2D approaches (11) and (16) for the boundary-value problem of the cantilever-bending due to their self weight of plates that are made of the elastomer VPS – whose density, again, is $\rho = 1148\ \mathrm{kg/m^3}$ and whose elasticity is characterized by the isotropic modulus of elasticity (8) with Lamé constants (7) – and have the 12 classes of perforated

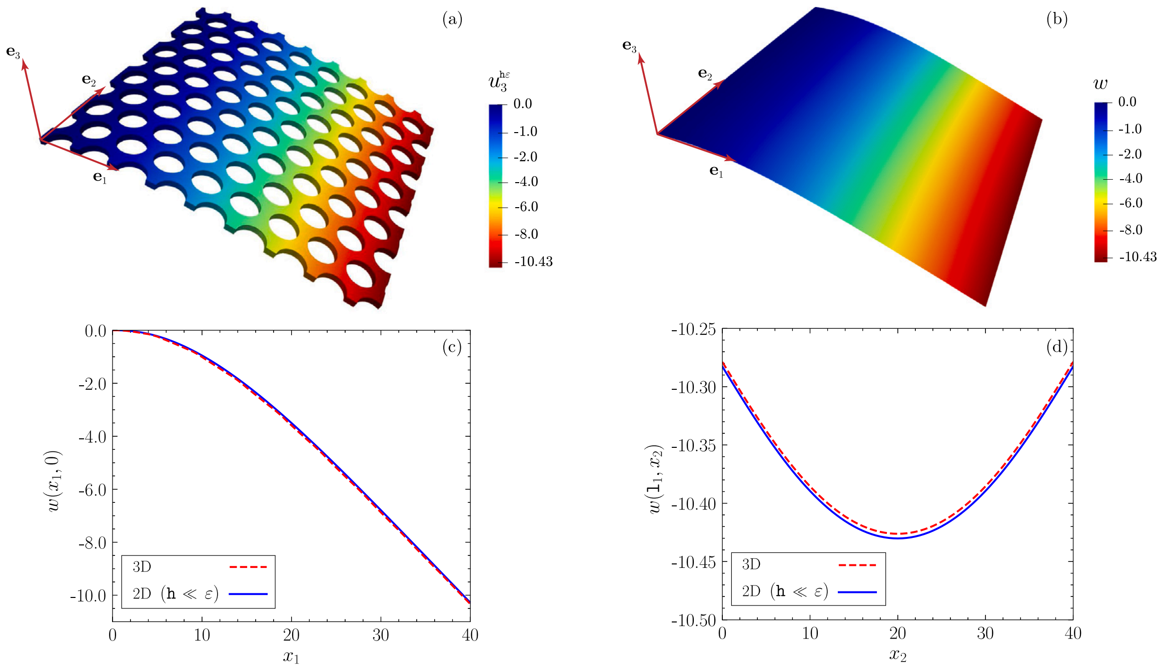

Fig. 3. Comparison between the solutions generated by the 3D approach (10) and the 2D approach (11) for the cantilever-bending response due to its self weight of a VPS plate with dimensions $\mathtt{l}_1 = 40$ mm, $\mathtt{l}_2 = 40$ mm, $\mathtt{h} = 0.8$ mm, and a hexagonal distribution of circular holes with porosity $f = 0.50$; all quantities are shown in mm. The 3D result (part (a) and dashed lines) corresponds to a plate with unit-cell size of $\varepsilon = 9.24$ mm.

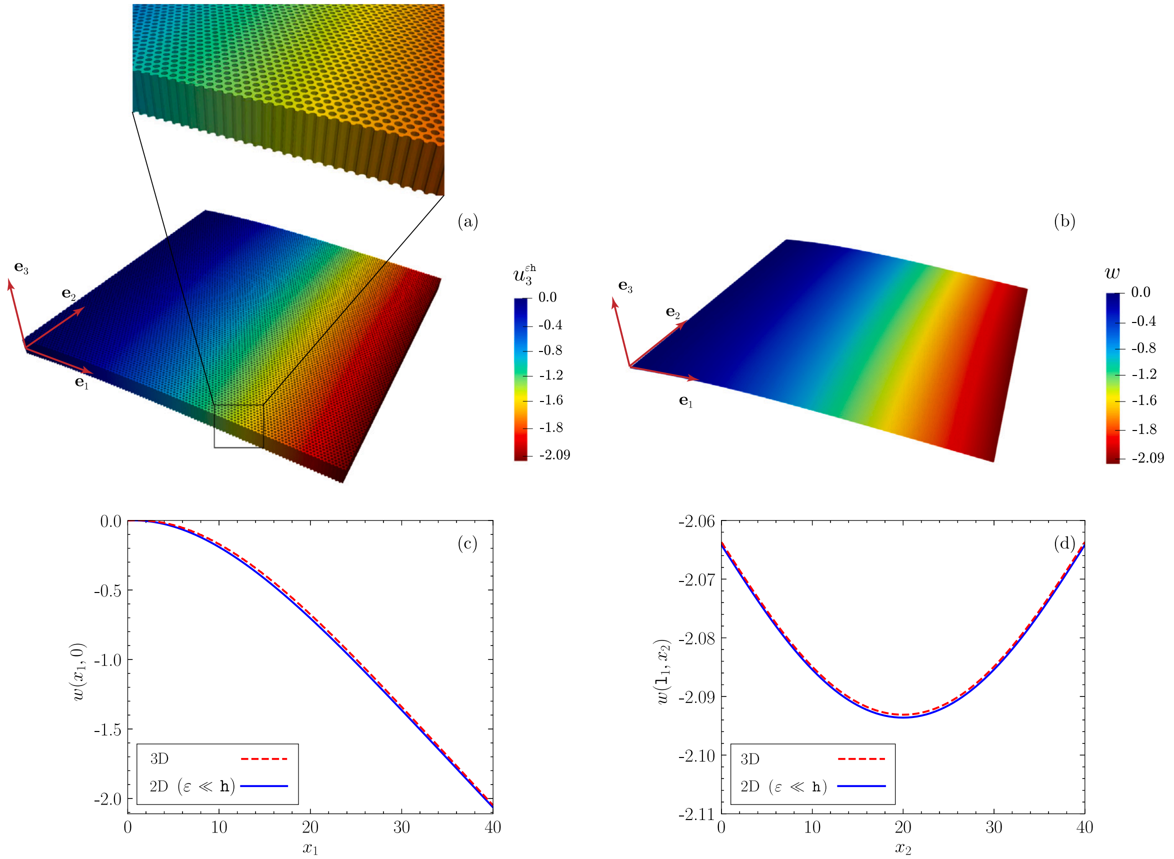

Fig. 4. Comparison between the solutions generated by the 3D approach (10) and the 2D approach (16) for the cantilever-bending response due to its self weight of a VPS plate with dimensions $\mathtt{l}_1 = 40$ mm, $\mathtt{l}_2 = 40$ mm, $\mathtt{h} = 2$ mm, and a hexagonal distribution of circular holes with porosity $f = 0.50$; all quantities are shown in mm. The 3D result (part (a) and dashed lines) corresponds to a plate with unit-cell size of $\varepsilon = 0.39$ mm.

microstructures listed in Table 1. A parametric study[1] based on those comparisons indicates that the 2D formulation (11) for plates whose thicknesses are much smaller than their heterogeneities is applicable whenever

$$\varepsilon \leq \frac{1}{4}\min\{\mathtt{l}_1, \mathtt{l}_2\} \qquad \text{and} \qquad \mathtt{h} \leq \frac{1}{5}\varepsilon. \tag{21}$$

On the other hand, the 2D formulation (16) for plates whose heterogeneities are much smaller than their thicknesses is applicable whenever

$$\mathtt{h} \leq \frac{1}{4}\min\{\mathtt{l}_1, \mathtt{l}_2\} \qquad \text{and} \qquad \varepsilon \leq \frac{1}{5}\mathtt{h}. \tag{22}$$

For illustration purposes, Fig. 3 presents a representative comparison between the solution generated by the 3D approach (10) and that generated by the 2D approach (11) for a VPS plate with a hexagonal distribution of circular holes aligned with the principal directions of the plate itself, that is, $\mathbf{e}'_\alpha = \mathbf{e}_\alpha$. Specifically, the results pertain to a plate with dimensions $\mathtt{l}_1 = 40$ mm, $\mathtt{l}_2 = 40$ mm, thickness $\mathtt{h} = 0.8$ mm, and porosity $f = 0.50$. For the 3D solution, moreover, the result corresponds to a unit-cell size of $\varepsilon = 9.23$ mm, so that $\varepsilon = \mathtt{l}_2/4.33$ and $\mathtt{h} = \varepsilon/11.5$, which satisfy the inequalities (21). Parts (a) and (b) of the figure show the deformed configurations of the plate, as determined from the 3D and 2D solutions, respectively. Parts (c) and (d) compare the 3D and 2D solutions for the displacement w of the midplane of the plate at $x_2 = 0$ along the $\mathbf{e}_1$ direction and at $x_1 = \mathtt{l}_1$ along the $\mathbf{e}_2$ direction, that is, $w(x_1, 0)$ and $w(\mathtt{l}_1, x_2)$, respectively.

In complete analogy with Fig. 3, Fig. 4 presents a representative comparison between the solution generated by the 3D approach (10) and that generated by the 2D approach (16). The results pertain to a plate with dimensions $\mathtt{l}_1 = 40$ mm, $\mathtt{l}_2 = 40$ mm, thickness $\mathtt{h} = 2$ mm, and porosity $f = 0.50$. In this case, for the 3D solution, the result corresponds to a unit-cell size of $\varepsilon = 0.39$ mm, so that $\mathtt{h} = \mathtt{l}_2/20$ and $\varepsilon = \mathtt{h}/5.19$, which satisfy the inequalities (22).

[1] The bounds (21) and (22) were determined from cantilever-bending responses due to self weight of perforated plates with thicknesses in the range $\mathtt{h} \in [0.5, 2]$ mm and unit-cell sizes in the range $\varepsilon \in [0.35, 12]$ mm.

It is clear from both sets of comparisons presented in Figs. 3 and 4 that the 2D plate theories (11) and (16) deliver solutions that are in good quantitative agreement with that of the full 3D theory (10).

5. Sensitivity to the order of the dimension-reduction and homogenization limits: $\mathtt{h} \ll \varepsilon$ vs $\varepsilon \ll \mathtt{h}$

The drastically different formulas (12) and (17) for the effective bending stiffness tensors $\widehat{\mathbf{M}}$ and $\widetilde{\mathbf{M}}$ put forth in Sections 3.2 and 3.3 in the opposite limiting case when $\mathtt{h} \ll \varepsilon$ and $\varepsilon \ll \mathtt{h}$ make it plain that the bending response of a thin perforated plate depends – in principle, strongly – on whether its thickness $\mathtt{h}$ is larger or smaller than its heterogeneity ε. In the sequel, with the objective of *quantifying* such a dependence, we confront to one another the effective bending stiffness tensors $\widehat{\mathbf{M}}$ and $\widetilde{\mathbf{M}}$ for plates that once more, as in the preceding section, are made of the elastomer VPS and feature the 12 classes of perforated microstructures listed in Table 1.

We begin by noting that all 12 types of plates in Table 1 are orthotropic and have $\mathbf{e}_1'$ and $\mathbf{e}_2'$ as principal directions. Accordingly, with respect to $\{\mathbf{e}_\alpha'\}$, $\widehat{M}_{1112} = \widehat{M}_{2212} = \widetilde{M}_{1112} = \widetilde{M}_{2212} = 0$. Tables 2 through 13 in the Appendix provide the values of the four remaining non-zero components of $\widehat{\mathbf{M}}$ and $\widetilde{\mathbf{M}}$ for all considered porosities in the range $f \in [0, 0.60]$. From those results, one can establish that

$$\widehat{\mathbf{M}} > \widetilde{\mathbf{M}} \tag{23}$$

in the sense of quadratic forms, that is, $\Xi \cdot \widehat{\mathbf{M}}\Xi > \Xi \cdot \widetilde{\mathbf{M}}\Xi$ for all non-zero $\Xi \in \mathbb{R}^2 \times \mathbb{R}^2$. In other words, irrespectively of the class of microstructure being considered, both the "pure bending" and "twisting" stiffnesses of a perforated plate whose thickness is smaller than its heterogeneity are greater than the "pure bending" and "twisting" stiffnesses of a corresponding (with the same thickness and class of microstructure) perforated plate whose heterogeneity is smaller than its thickness.

In order to gain quantitative insight into the inequality (23), we plot the relative difference

$$\Delta\overline{M}_{\alpha\beta\gamma\delta} := \frac{\widehat{M}_{\alpha\beta\gamma\delta} - \widetilde{M}_{\alpha\beta\gamma\delta}}{\widehat{M}_{\alpha\beta\gamma\delta}} \qquad \text{(no summation)} \tag{24}$$

in Figs. 5 and 6 for the plates with both the square and hexagonal distributions of holes, respectively. The data is shown in absolute value in the form of bar plots as a function of the porosity. There are two key observations that can be readily made from these figures.

The first one is that the relative differences between the "pure bending" components $\widehat{M}_{1111}$, $\widehat{M}_{2222}$ and $\widetilde{M}_{1111}$, $\widetilde{M}_{2222}$ remain remarkably small even for plates with large porosities near their percolation limit. This is particularly true for plates with the square distributions of holes for which these relative differences do not exceed 5%. For most of the plates with the hexagonal distributions of holes, the same relative differences remain well below 20%. Larger differences do appear, however, for the plates with rectangular

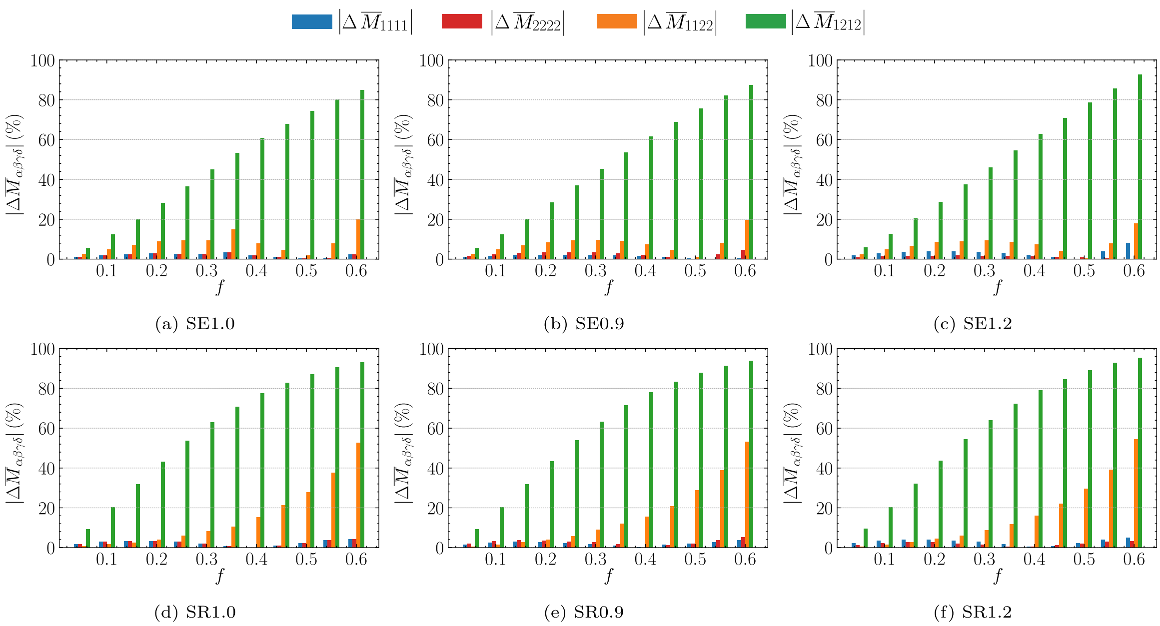

Fig. 5. Relative difference (24) between the effective bending stiffness tensors $\widehat{\mathbf{M}}$ and $\widetilde{\mathbf{M}}$ for plates made of VPS with square distributions of elliptical (SE) and rectangular holes (SR); see Table 1 for the labels of the different microstructures. The results are shown in absolute value as a function of the porosity f of the plates.

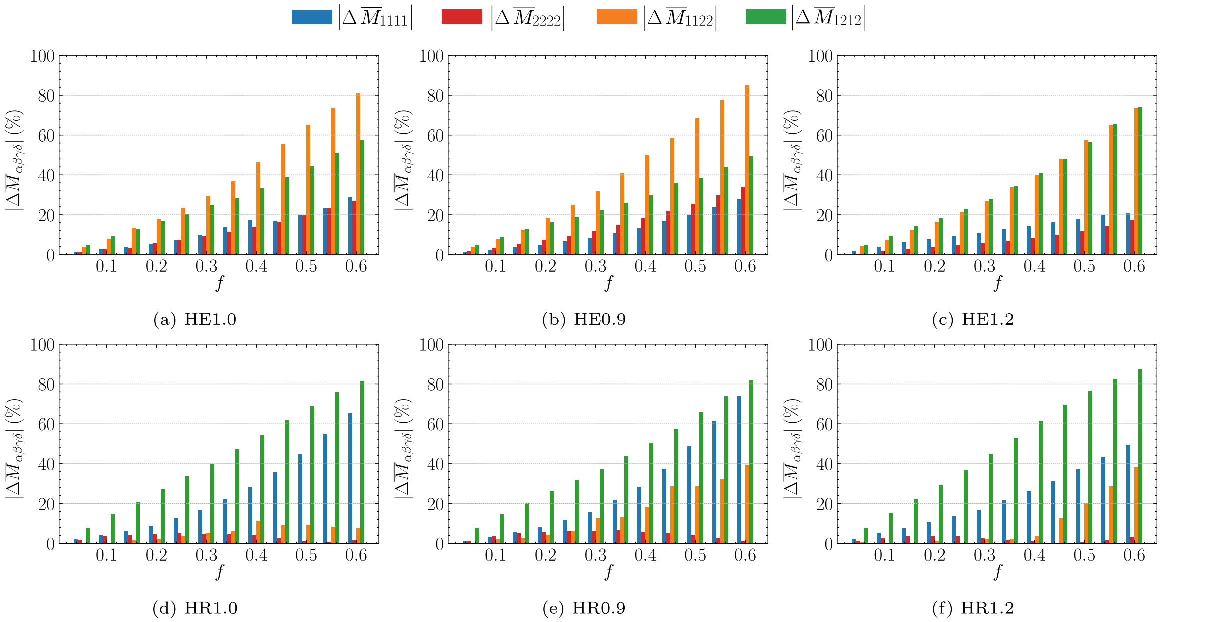

Fig. 6. Relative difference (24) between the effective bending stiffness tensors $\widehat{\mathbf{M}}$ and $\widetilde{\mathbf{M}}$ for plates made of VPS with hexagonal distributions of elliptical (HE) and rectangular (HR) holes; see Table 1 for the labels of the different microstructures. The results are shown in absolute value as a function of the porosity f of the plates.

holes as their volume fractions approach percolation. We make special mention of the results $\Delta\overline{M}_{1111} = \Delta\overline{M}_{2222} \approx 20\%$ for the HE1.0 plates with the hexagonal distributions of circular holes at $f = 0.50$, which were precisely the types of plates used by Pezzulla et al. (2020). These results provide an explanation for their observations that plates with the same thickness and porosity but very different hole sizes bent in similar manner when towed through a fluid bath.

The second key observation from Figs. 5 and 6 is that the relative difference between the "twisting" components $\widehat{M}_{1212}$ and $\widetilde{M}_{1212}$, and to a lesser extent that between $\widehat{M}_{1122}$ and $\widetilde{M}_{1122}$, is sizable and scales roughly linearly with the porosity.

6. Sensitivity to the porosity, spatial distribution, and shape of the holes

The opposite limiting results (h$\ll \varepsilon$ vs. $\varepsilon \ll$h) put forth in Sections 3.2 and 3.3 make it equally plain that the bending response of a thin perforated plate depends as well on the specifics of its microstructure, namely, the porosity, spatial distribution, and shape of its holes. In this section, we quantify such dependencies.

We begin by quantifying the dependence on the porosity. To that end, we consider the relative differences

$$\delta\widehat{M}_{\alpha\beta\gamma\delta} := \frac{M_{\alpha\beta\gamma\delta} - \min_{\{\mathrm{SE,SR,HE,HR}\}}\left\{\widehat{M}_{\alpha\beta\gamma\delta}\right\}}{M_{\alpha\beta\gamma\delta}} \qquad \text{(no summation)} \tag{25}$$

and

$$\delta\widetilde{M}_{\alpha\beta\gamma\delta} := \frac{M_{\alpha\beta\gamma\delta} - \min_{\{\mathrm{SE,SR,HE,HR}\}}\left\{\widetilde{M}_{\alpha\beta\gamma\delta}\right\}}{M_{\alpha\beta\gamma\delta}} \qquad \text{(no summation)}, \tag{26}$$

which provide measures of how much the effective bending stiffness tensors $\widehat{\mathbf{M}}$ and $\widetilde{\mathbf{M}}$ deviate from the bending stiffness tensor $\mathbf{M}$ of the matrix material, among all considered microstructures with square (S) and hexagonal (H) distributions of elliptical (E) and rectangular (R) holes, upon the addition of porosity f. Fig. 7 plots values for both of these measures, in the form of bar plots as functions of f, for the same type of VPS plates examined in the preceding sections.

In order to quantify the effects of the spatial distribution and shape of the holes, we further consider the relative differences

$$\Delta\widehat{M}_{\alpha\beta\gamma\delta} := \frac{\max_{\{\mathrm{SE,SR,HE,HR}\}}\left\{\widehat{M}_{\alpha\beta\gamma\delta}\right\} - \min_{\{\mathrm{SE,SR,HE,HR}\}}\left\{\widehat{M}_{\alpha\beta\gamma\delta}\right\}}{M_{\alpha\beta\gamma\delta}} \qquad \text{(no summation)} \tag{27}$$

and

$$\Delta\widetilde{M}_{\alpha\beta\gamma\delta} := \frac{\max_{\{\mathrm{SE,SR,HE,HR}\}}\left\{\widetilde{M}_{\alpha\beta\gamma\delta}\right\} - \min_{\{\mathrm{SE,SR,HE,HR}\}}\left\{\widetilde{M}_{\alpha\beta\gamma\delta}\right\}}{M_{\alpha\beta\gamma\delta}} \qquad \text{(no summation)}, \tag{28}$$

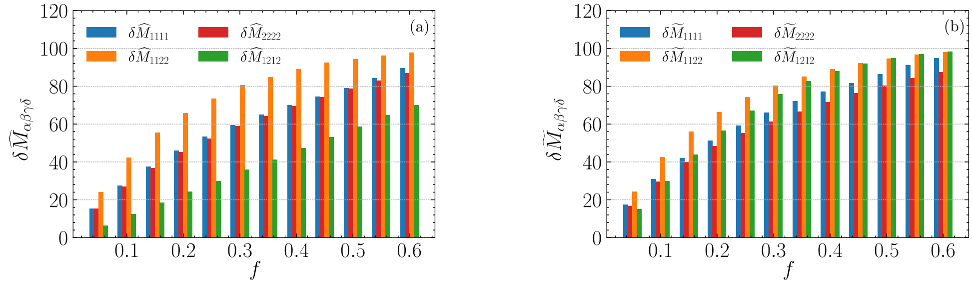

Fig. 7. Relative differences (25) and (26) between the effective bending stiffness tensors (a) $\widehat{\mathbf{M}}$ and (b) $\widetilde{\mathbf{M}}$ and the matrix bending stiffness tensor $\mathbf{M}$ for the same 12 types of perforated VPS plates considered in Figs. 5 and 6. The results are shown as a function of the porosity f of the plates.

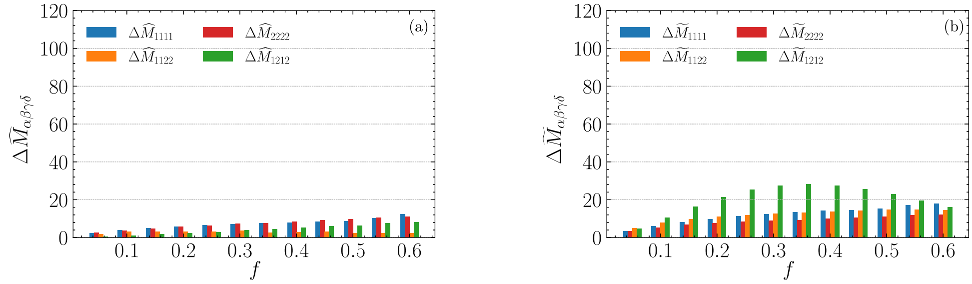

Fig. 8. Relative differences (27) and (28) of the effective bending stiffness tensors (a) $\widehat{\mathbf{M}}$ and (b) $\widetilde{\mathbf{M}}$ among themselves for the same 12 types of perforated VPS plates considered in Figs. 5 and 6. The results are shown as a function of the porosity f of the plates.

which provide measures of how much deviation the effective bending stiffness tensors $\widehat{\mathbf{M}}$ and $\widetilde{\mathbf{M}}$ exhibit among themselves for plates with the same porosity but different microstructures. The normalization in the measures (27) and (28) is done with respect to the bending stiffness tensor $\mathbf{M}$ of the matrix material so as to make them directly comparable with (25) and (26). Similar to Fig. 7, Fig. 8 presents plots of (27) and (28) in the form of bar plots as functions of f.

Noting that they show identical ranges of values (from 0% to 120%), a quick glance at Figs. 7 and 8 suffices to recognize that the relative quantity of holes – namely, the porosity – that is added to a thin plate has a much more significant impact on its bending response than the spatial distribution and shape of those holes, irrespectively of whether their size is smaller or larger than the plate thickness.

7. Experiments

7.1. Fabrication of the samples

Material. We use the silicone-based elastomer Vinyl Polysiloxane (VPS-32, Zhermack) to make all the plates that are investigated experimentally in this work. In addition to its commercial availability, this material is chosen because it can be easily molded into any desired shape. In its fully cured state, as already noted in Section 3.1 above, the density and Young's modulus of VPS are $\rho = 1148\ \mathrm{kg/m^3}$ and $E = 1.3$ MPa. The Young's modulus was measured using standard tensile tests on dogbone specimens. Its Poisson's ratio was not measured. In the simulations we assume it to be $\nu = 0.46$, reflecting the near incompressibility of VPS.

Fabrication of the molds. The plates were fabricated by means of a casting process. Specifically, they were cast between two acrylic slabs, one flat and the other engraved with the desired pattern; see (*i*) and (*ii*) in Fig. 9(a). The engraved slabs were themselves fabricated by using the engraving capabilities of a Speedy 400 Laser Cutter/Engraver (Trotec Laser AG). The desired engraving depth was achieved by suitably adjusting the laser speed and power (respectively 15% and 40% of their maximal value). The engraving produced dust and residues which were removed by first blowing compressed air onto the slab, submerging it into a sonic bath for 90 min, and finally using pliers to remove any remaining residue. The engraved portion of the slab consisted of a $40\,\mathrm{mm} \times 40\,\mathrm{mm}$ area featuring the desired pattern and an additional $20\,\mathrm{mm} \times 40\,\mathrm{mm}$ area without engraving that served to cast the part of the plates that was clamped during their testing; see (*iii*) in Fig. 9(a).

Molding of the plates. In order to fabricate the plates, the base and catalyst components of VPS were first mixed with a 1:1 weight ratio using a THINKY ARE-250 mixer at $2000\,\mathrm{rpm}$ clockwise for 10 s and $2200\,\mathrm{rpm}$ counterclockwise for 10 s. The liquid elastomer mixture was then poured onto the engraved slab and subsequently degassed by placing it under $30\,\mathrm{mbar}$ for 15 s. The flat slab was then carefully placed on top so as to avoid the formation of air bubbles in the specimen. The bottom and top slabs were tightly pressed against each other using four screws located at their corners. After one week at room temperature, which is long enough

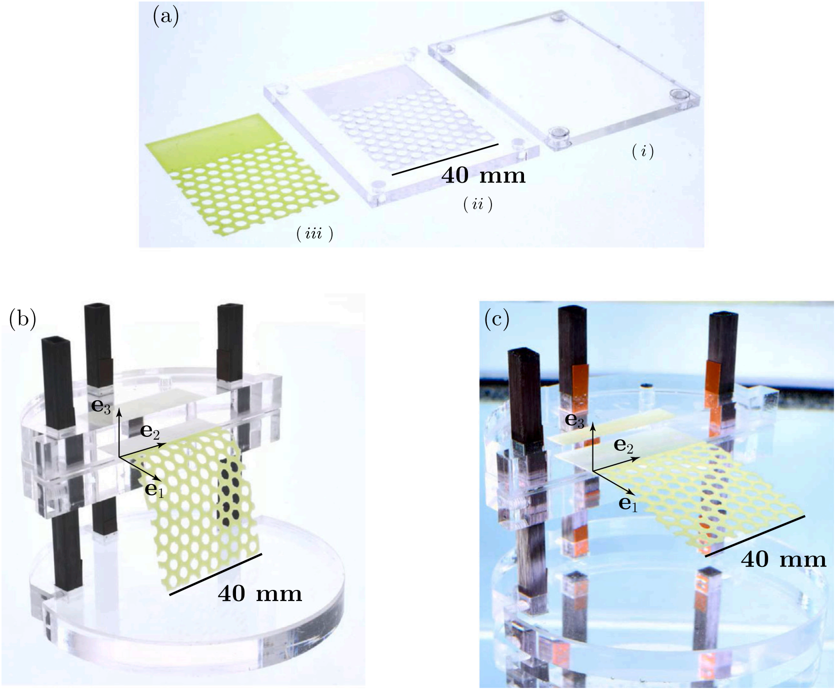

Fig. 9. (a) Photograph of one of the molds used for the fabrication of the perforated plates showing (*i*) the top flat acrylic slab, (*ii*) the bottom acrylic slab with the engraved pattern, and (*iii*) the resulting perforated VPS plate obtained after curing. (b) The cantilever set-up that is immersed in water and placed inside the μCT; the deflection of the perforated plate shown in this figure is enormous because the set-up is not yet immersed in water. (c) The same set-up immersed in water, showing the large but not enormous deflection of the plate.

for VPS to fully cure and attain stable mechanical properties, the plates were finally taken out of the mold for testing. Prior to the cantilever-bending tests, the thickness h of the plates was measured.

7.2. Cantilever-bending of the plates and their X-ray tomographic characterization

The response of the fabricated plates was probed by subjecting them to cantilever bending under self weight. With the objective of avoiding exceedingly large deformations in the VPS elastomer, the tests were carried out with the plates entirely immersed in water, which effectively results in an environment where the acceleration of gravity is $g = (\rho - \rho_{water})g_0/\rho = 1.27$ m/s^2 instead of $g_0 = 9.81$ m/s^2; see Figs. 9(b) and (c) for the set-up in air and immersed in water.

The chosen dimensions of the plates were such that, together with the holding apparatus, they fitted into the Scanco Medical micro-tomography scanner (μCT 100 HE) used to carry out the measurements of their cantilever bending. The holding apparatus was non-metallic and consisted of two acrylic slabs in between which the plates were clamped. This clamp was supported by three squared carbon fiber pillars whose heights could be adjusted; see Figs. 9(b) and (c). The whole set-up was placed in the μCT's sample holder (a cylinder with an inner diameter of 100 mm and height of 100 mm) and immersed in water. In the laboratory frame of reference $\{\mathbf{e}_i\}$, the gravitational field is in the $-\mathbf{e}_3$ direction and the clamped part of the plate lies in the $\{\mathbf{e}_1, \mathbf{e}_2\}$ plane. A bi-directional level was used to minimize misalignment. Furthermore, to avoid the formation of air bubbles during the measurements, the air naturally dissolved in the water was removed by placing the immersed set-up under 20 mbar for 30 min.

The μCT parameters used for the scans are the following: voltage 55 kVp, current 200 μA, aluminum filter of thickness 0.5 mm, and an integration time of 801 ms. A full scan lasted for approximately 2 h. The resulting scans consist of 1000-to-2000 grayscale images stacked in the $\mathbf{e}_3$ direction, with a distance of 34.2 µm between each slice. Each image lies in the $\{\mathbf{e}_1, \mathbf{e}_2\}$ plane and is composed of 3072 × 3072 pixels with also a spatial resolution of 34.2 µm. The voxel size of the 3D scan is thus 34.2 µm in all three directions.

Volume and deformation analysis of the plates. In order to reconstruct the full image of a perforated plate and measure its deformation, the stack of images collected from the scan was first imported to the processing program ImageJ (ImageJ 1.52b, National Institutes of Health). Using this software, the domain of interest was first identified. Then, as illustrated by Figs. 10(a) and (b), a Gaussian filter with a 3 pixel radius was applied to remove high frequency noise from the raw images. Finally, an intensity threshold was applied to create a binarized volume – where voxels with the value of 1 identify the regions occupied by the VPS material, while voxels with the value of 0 identify the remaining regions – that isolated the plate from the surrounding water and holding apparatus.

Subsequently, in order to quantify the deformation of the plate, we imported the binarized volume to the Imaging Processing Toolbox in MATLAB (see MATLAB R2019A Version Documentation, 2019). There, we first selected the frame of reference to coincide

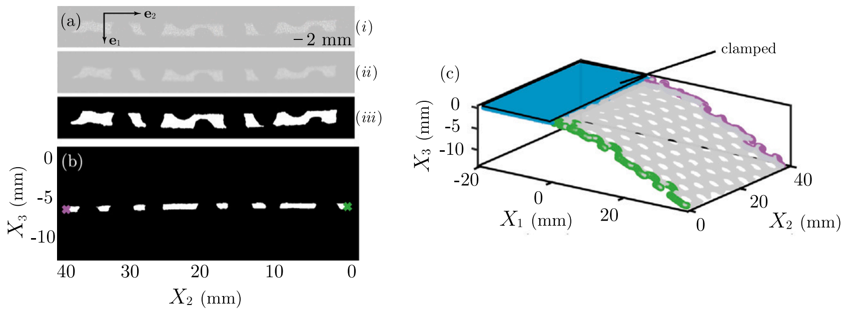

Fig. 10. (a) Schematic of the image processing protocol followed to extract the deformation of the perforated plates from the μCT images. For each grayscale slice in the $\{\mathbf{e}_1, \mathbf{e}_2\}$ plane, the raw image (*i*) was passed through a Gaussian filter to remove high intensity noise in the background and then the filtered image (*ii*) was binarized by using an intensity threshold (*iii*). (b) For each slice in the $\{\mathbf{e}_1, \mathbf{e}_3\}$ plane, the position of the two edges were detected (purple and green crosses). (c) Reconstructed perforated plate from the μCT data, with the clamped part ($X_1 < 0$) colored in blue and the two edges along the $\mathbf{e}_1$ direction colored in green and purple.

with the laboratory frame of reference; see Fig. 10(c). We proceeded by determining the location of the deformed edges of the plate at $x_2 = 0$ and $x_2 = \mathtt{l}_2$ along the $\mathbf{e}_1$ direction. To do so, we considered $\{\mathbf{e}_1, \mathbf{e}_3\}$ slices of the volume and, for each slice, we identified the points where the apparent thickness first and last reached 80% of the plate's thickness. This results in two sets of points running along the two lateral edges of the plate; see Fig. 10(b). The $\mathbf{e}_3$ components of these points correspond to the displacements $w(x_1, 0)$ and $w(x_1, \mathtt{l}_2)$ of the lateral edges of the plate's midplane, with an uncertainty given by the thickness of the plate. The small changes in the locations of the material points along the $\mathbf{e}_1$ direction before and after deformation are neglected.

8. Theory vs. experiments

In the sequel, we compare the experiments described in the preceding section with the corresponding 2D theoretical predictions. All the comparisons pertain to plates with dimensions $\mathtt{l}_1 = 40$ mm, $\mathtt{l}_2 = 40$ mm, $\mathtt{h} = 0.73$ mm, embedding a hexagonal distribution of elliptical holes with aspect ratio $\omega = 0.9$ that are aligned at 45° with respect to the plates' principal axes, that is, $\mathbf{e}_1' = 1/\sqrt{2}(\mathbf{e}_1 + \mathbf{e}_2)$

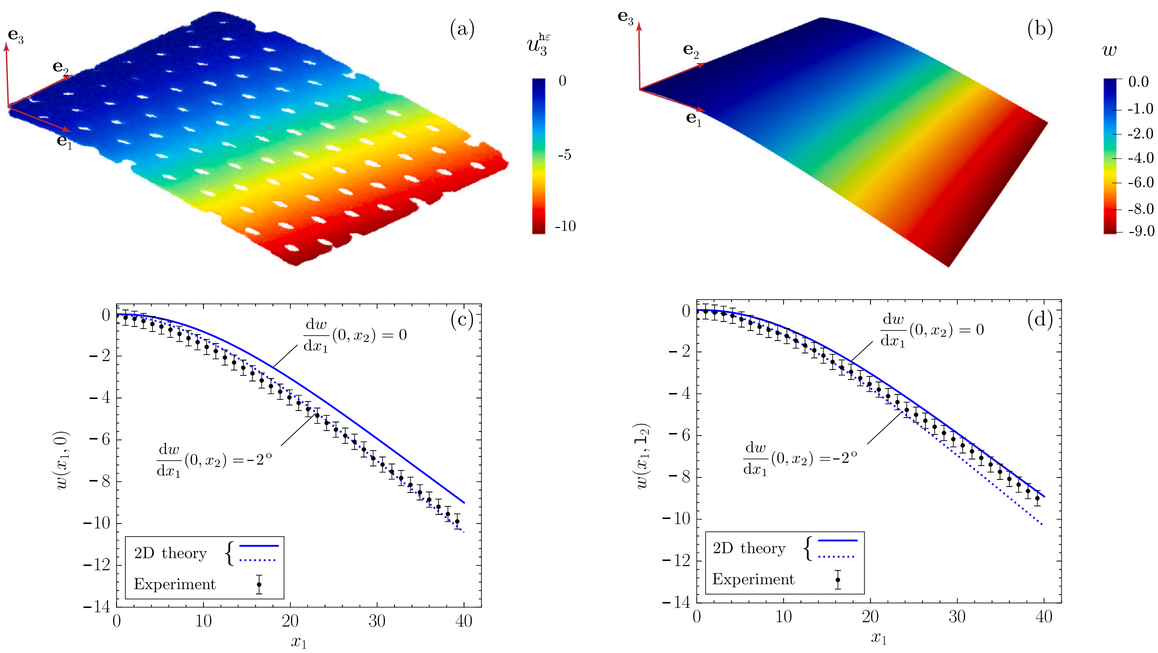

Fig. 11. Comparison between experimental measurements and the prediction generated by the 2D theory (11) for the cantilever-bending response due to its self weight of a VPS plate with dimensions $\mathtt{l}_1 = 40$ mm, $\mathtt{l}_2 = 40$ mm, $\mathtt{h} = 0.73$ mm, and a hexagonal distribution of elliptical holes with aspect ratio $\omega = 0.9$ and porosity $f = 0.20$; all quantities are shown in mm. The comparisons shown in parts (c) and (d) correspond to the displacement w of the midplane of the plate at $x_2 = 0$ and $x_2 = \mathtt{l}_2$ along the $\mathbf{e}_1$ direction, that is, $w(x_1, 0)$ and $w(x_1, \mathtt{l}_2)$.

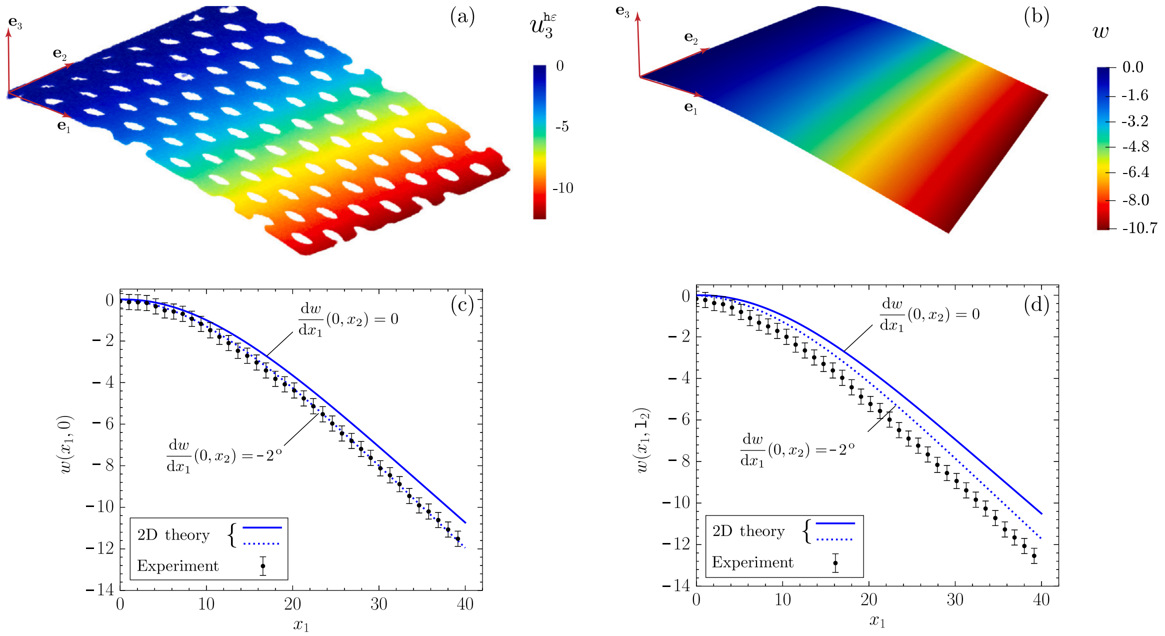

Fig. 12. Comparison between experimental measurements and the prediction generated by the 2D theory (11) for the cantilever-bending response due to its self weight of a VPS plate with dimensions $l_1 = 40$ mm, $l_2 = 40$ mm, $h = 0.73$ mm, and a hexagonal distribution of elliptical holes with aspect ratio $\omega = 0.9$ and porosity $f = 0.35$; all quantities are shown in mm. The comparisons shown in parts (c) and (d) correspond to the displacement w of the midplane of the plate at $x_2 = 0$ and $x_2 = l_2$ along the $\mathbf{e}_1$ direction, that is, $w(x_1, 0)$ and $w(x_1, l_2)$.

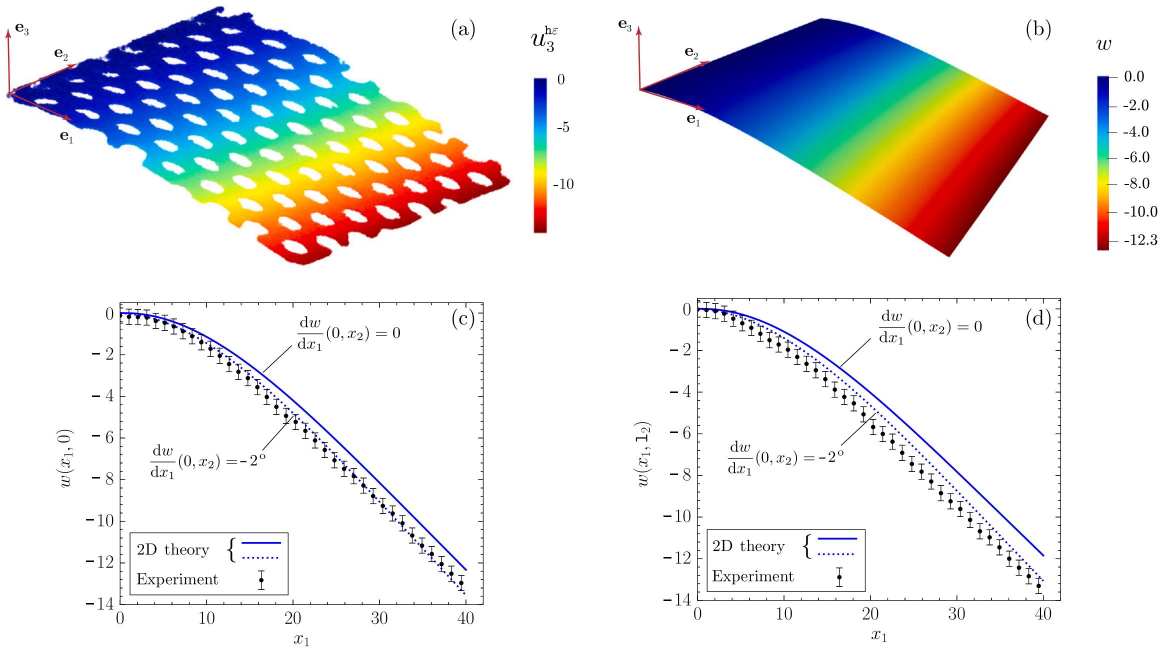

Fig. 13. Comparison between experimental measurements and the prediction generated by the 2D theory (11) for the cantilever-bending response due to its self weight of a VPS plate with dimensions $l_1 = 40$ mm, $l_2 = 40$ mm, $h = 0.73$ mm, and a hexagonal distribution of elliptical holes with aspect ratio $\omega = 0.9$ and porosity $f = 0.50$; all quantities are shown in mm. The comparisons shown in parts (c) and (d) correspond to the displacement w of the midplane of the plate at $x_2 = 0$ and $x_2 = l_2$ along the $\mathbf{e}_1$ direction, that is, $w(x_1, 0)$ and $w(x_1, l_2)$.

and $\mathbf{e}_2' = 1/\sqrt{2}(-\mathbf{e}_1 + \mathbf{e}_2)$. We choose to examine a *rotated configuration* of an *anisotropic microstructure* in order to expediently probe both the "pure bending" and "pure twisting" responses of the plate in a single test. The size of the unit cell in all the experiments is $\varepsilon = 9.24$ mm, which together with the size $\mathtt{h} = 0.73$ mm of the thickness satisfy the string of inequalities (21), thus the use of the 2D theory (11) for the comparisons (see Section 4).

Fig. 11 shows comparisons for a plate with porosity $f = 0.20$. Parts (a) and (b) of the figure show the deformed configurations of the plate, as determined from the X-ray tomography measurements and theory, respectively. Parts (c) and (d) compare the results for the displacement w of the midplane of the plate at $x_2 = 0$ and $x_2 = \mathtt{l}_2$ along the $\mathbf{e}_1$ direction, that is, $w(x_1, 0)$ and $w(x_1, \mathtt{l}_2)$, respectively. The similarity in densities of VPS and water (wherein, again, the plates are immersed) makes it difficult to differentiate points across the thickness of the plates in the X-ray tomography measurements. The error bars (± 0.36 mm) in the plots describe this uncertainty. In the experiment, moreover, the angle at which the plate is clamped is not exactly zero. To illustrate the effect of this deviation from perfect alignment, the theoretical prediction for the case when $\mathrm{d}w(x_1, 0)/\mathrm{d}x_1 = -2°$ is also included in parts (c) and (d) of the comparison. Figs. 12 and 13 show comparisons entirely analogous to those presented by Fig. 11 for plates with the larger porosities $f = 0.35$ and 0.50.

The following comments are in order from the above three sets of comparisons. First, the theory is in fairly good quantitative agreement with the experiments. Second, and rather interestingly, the overall displacement of the plates is seen to increase sizably with increasing porosity from $f_0 = 0.20$, to 0.35, to 0.50. This implies that the decrease in effective bending stiffness trumps the competing decrease in self-weight that result from the addition of holes to the plates. Finally, the overall anisotropic bending stiffness that results from the elliptical shape of the holes is noticeable as demonstrated by the differences (up to 4% for the plate with porosity $f_0 = 0.50$) between the displacement w of the plates along their opposite edges $x_2 = 0$ and $x_2 = \mathtt{l}_2$.

9. Final comments

Motivated by the intriguing mechanical responses of porous strips towed through a fluid bath that were recently reported by Pezzulla et al. (2020), we have carried out a detailed analysis of the bending response of thin perforated plates made of a homogeneous isotropic material embedding square and hexagonal periodic distributions of monodisperse elliptical and rectangular holes with a large range of porosities. The analysis has brought to light several conclusions of fundamental and practical relevance.

- First and foremost, the bending response of thin perforated plates is dominated by the relative quantity of holes that they contain – that is, by the porosity – and, counter to the general expectation from available mathematical results for heterogeneous plates at large, *not* by whether the holes are smaller or larger than the plate thickness nor by their spatial distribution or shape.
- The secondary effects due to the relative difference between plate thickness and hole size are greater for the "twisting" response of the plates than for their "pure bending" response. Interestingly enough, both the "pure bending" and "twisting" responses of a thin perforated plate whose thickness is smaller than its holes are consistently greater than the "pure bending" and "twisting" responses of a corresponding (with identical thickness and class of microstructure) perforated plate whose holes are smaller than its thickness.
- Provided that the strains remain within the linear elastic regime of the underlying matrix material, thin perforated plates can be effectively modeled as 2D structures made of a homogeneous elastic material already when their thicknesses and hole sizes are only 4-to −5 times smaller than their in-plane dimensions; see Eqs. (21) and (22).

The dominance of the porosity in the bending properties of perforated plates is consistent with the mechanical properties that have been recently reported for other types of porous material systems, such as porous elastomers and syntactic foams (Shrimali et al., 2019, 2020). In all such systems, the dominance of the porosity can be attributed to the fact that the underlying holes are "infinitely softer" that the surrounding matrix material and hence the deformation localizes within them in proportion to their content without much regard to their spatial distribution and shape.

The finding that plates whose thicknesses are smaller than their holes are stiffer than corresponding plates whose holes are smaller than their thicknesses is a much less intuitive result than that of the dominance of the porosity. It may behoove analysts to rigorously establish whether the inequality (23) is universally applicable to all heterogeneous plates.

In closing, we return to the work by Pezzulla et al. (2020) that motivated the present study. Our theoretical analysis, which was validated experimentally, rationalizes the empirical observation by Pezzulla et al. (2020) that the bending stiffness of perforated plates is nearly insensitive to whether the holes are smaller or larger than the plate thickness, as long as the porosity remains fixed. From a practical standpoint, these findings could be leveraged as a design guideline, now under a predictive framework, for fluid–structure interaction applications involving perforated plates, for example, under a weight-minimization constraint. Furthermore, these results could facilitate the design of plate-like perforated structures where larger holes may be favored over smaller ones at the fabrication stage.

CRediT authorship contribution statement

Bhavesh Shrimali: Conceptualization, Methodology, Software, Writing - review & editing. **Matteo Pezzulla:** Methodology, Validation, Investigation, Writing - review & editing. **Samuel Poincloux:** Methodology, Validation, Formal analysis, Investigation, Writing - review & editing. **Pedro M. Reis:** Conceptualization, Methodology, Resources, Supervision, Writing - review & editing. **Oscar Lopez-Pamies:** Conceptualization, Methodology, Supervision, Funding acquisition, Writing - original draft, Writing - review & editing.

Declaration of competing interest

The authors declare that they have no known competing financial interests or personal relationships that could have appeared to influence the work reported in this paper.

Acknowledgment

The theoretical and computational aspects of this work were supported by the National Science Foundation through the grant CMMI–1901583.

Appendix. The effective bending tensors $\widehat{\mathrm{M}}$ and $\widetilde{\mathrm{M}}$ for VPS plates with the 12 perforated microstructures listed in Table 1.

Table 2
The effective bending stiffness tensors (12) and (17) for VPS plates with microstructure SE0.9. The results are shown normalized by the bending stiffness (13) of the underlying VPS matrix material.

f	$\frac{\widehat{M}_{1111}}{M_{1111}}$	$\frac{\widehat{M}_{2222}}{M_{2222}}$	$\frac{\widehat{M}_{1122}}{M_{1122}}$	$\frac{\widehat{M}_{1212}}{M_{1212}}$	$\frac{\widetilde{M}_{1111}}{M_{1111}}$	$\frac{\widetilde{M}_{2222}}{M_{2222}}$	$\frac{\widetilde{M}_{1122}}{M_{1122}}$	$\frac{\widetilde{M}_{1212}}{M_{1212}}$
0.05	0.869	0.861	0.775	0.943	0.861	0.847	0.796	0.888
0.1	0.762	0.747	0.605	0.887	0.75	0.729	0.637	0.776
0.15	0.673	0.653	0.475	0.834	0.66	0.633	0.51	0.666
0.2	0.597	0.572	0.373	0.781	0.584	0.553	0.407	0.56
0.25	0.531	0.501	0.293	0.731	0.52	0.484	0.323	0.461
0.3	0.474	0.439	0.229	0.68	0.463	0.424	0.253	0.371
0.35	0.422	0.382	0.178	0.63	0.414	0.371	0.196	0.292
0.4	0.375	0.33	0.137	0.579	0.369	0.323	0.148	0.223
0.45	0.332	0.281	0.103	0.527	0.328	0.278	0.108	0.165
0.5	0.292	0.235	0.076	0.474	0.29	0.235	0.075	0.115
0.55	0.255	0.189	0.054	0.418	0.255	0.193	0.049	0.075
0.6	0.22	0.144	0.035	0.358	0.221	0.151	0.028	0.045

Table 3
The effective bending stiffness tensors (12) and (17) for VPS plates with microstructure SE1.0. The results are shown normalized by the bending stiffness (13) of the underlying VPS matrix material.

f	$\frac{\widehat{M}_{1111}}{M_{1111}}$	$\frac{\widehat{M}_{2222}}{M_{2222}}$	$\frac{\widehat{M}_{1122}}{M_{1122}}$	$\frac{\widehat{M}_{1212}}{M_{1212}}$	$\frac{\widetilde{M}_{1111}}{M_{1111}}$	$\frac{\widetilde{M}_{2222}}{M_{2222}}$	$\frac{\widetilde{M}_{1122}}{M_{1122}}$	$\frac{\widetilde{M}_{1212}}{M_{1212}}$
0.05	0.865	0.865	0.775	0.942	0.854	0.854	0.797	0.889
0.1	0.755	0.755	0.607	0.887	0.74	0.74	0.638	0.777
0.15	0.663	0.663	0.475	0.833	0.647	0.647	0.512	0.667
0.2	0.586	0.586	0.373	0.782	0.569	0.569	0.409	0.561
0.25	0.517	0.517	0.294	0.73	0.503	0.503	0.325	0.463
0.3	0.458	0.458	0.231	0.68	0.445	0.445	0.255	0.374
0.35	0.407	0.407	0.168	0.632	0.394	0.394	0.197	0.295
0.4	0.353	0.353	0.138	0.579	0.347	0.347	0.15	0.227
0.45	0.308	0.308	0.105	0.527	0.304	0.304	0.11	0.169
0.5	0.266	0.266	0.076	0.473	0.265	0.265	0.078	0.122
0.55	0.225	0.225	0.056	0.419	0.227	0.227	0.051	0.083
0.6	0.186	0.186	0.038	0.36	0.19	0.19	0.031	0.055

Table 4
The effective bending stiffness tensors (12) and (17) for VPS plates with microstructure SE1.2. The results are shown normalized by the bending stiffness (13) of the underlying VPS matrix material.

f	$\frac{\widehat{M}_{1111}}{M_{1111}}$	$\frac{\widehat{M}_{2222}}{M_{2222}}$	$\frac{\widehat{M}_{1122}}{M_{1122}}$	$\frac{\widehat{M}_{1212}}{M_{1212}}$	$\frac{\widetilde{M}_{1111}}{M_{1111}}$	$\frac{\widetilde{M}_{2222}}{M_{2222}}$	$\frac{\widetilde{M}_{1122}}{M_{1122}}$	$\frac{\widetilde{M}_{1212}}{M_{1212}}$
0.05	0.858	0.872	0.776	0.943	0.842	0.864	0.795	0.888
0.1	0.741	0.766	0.604	0.887	0.72	0.757	0.635	0.775
0.15	0.645	0.68	0.474	0.834	0.621	0.668	0.508	0.664
0.2	0.561	0.603	0.37	0.782	0.539	0.594	0.404	0.557
0.25	0.488	0.541	0.291	0.73	0.469	0.531	0.32	0.457
0.3	0.423	0.484	0.226	0.68	0.408	0.476	0.25	0.367
0.35	0.364	0.434	0.175	0.63	0.353	0.427	0.192	0.286
0.4	0.31	0.389	0.133	0.579	0.303	0.383	0.144	0.215
0.45	0.258	0.347	0.1	0.527	0.256	0.344	0.104	0.154
0.5	0.209	0.31	0.071	0.476	0.21	0.307	0.071	0.102
0.55	0.157	0.274	0.048	0.416	0.164	0.273	0.044	0.059
0.6	0.103	0.24	0.028	0.352	0.113	0.241	0.023	0.025

Table 5
The effective bending stiffness tensors (12) and (17) for VPS plates with microstructure SR0.9. The results are shown normalized by the bending stiffness (13) of the underlying VPS matrix material.

f	$\frac{\widehat{M}_{1111}}{M_{1111}}$	$\frac{\widehat{M}_{2222}}{M_{2222}}$	$\frac{\widehat{M}_{1122}}{M_{1122}}$	$\frac{\widehat{M}_{1212}}{M_{1212}}$	$\frac{\widetilde{M}_{1111}}{M_{1111}}$	$\frac{\widetilde{M}_{2222}}{M_{2222}}$	$\frac{\widetilde{M}_{1122}}{M_{1122}}$	$\frac{\widetilde{M}_{1212}}{M_{1212}}$
0.05	0.858	0.85	0.761	0.938	0.845	0.834	0.757	0.851
0.1	0.746	0.732	0.586	0.881	0.727	0.708	0.577	0.702
0.15	0.653	0.633	0.455	0.825	0.634	0.61	0.442	0.562
0.2	0.575	0.549	0.353	0.771	0.559	0.53	0.34	0.437
0.25	0.509	0.479	0.277	0.718	0.497	0.465	0.261	0.331
0.3	0.452	0.421	0.219	0.668	0.445	0.409	0.199	0.245
0.35	0.404	0.366	0.171	0.62	0.4	0.359	0.151	0.177
0.4	0.358	0.316	0.133	0.569	0.359	0.316	0.112	0.126
0.45	0.318	0.272	0.102	0.521	0.323	0.276	0.081	0.087
0.5	0.284	0.234	0.079	0.476	0.289	0.239	0.056	0.058
0.55	0.251	0.197	0.059	0.428	0.258	0.204	0.036	0.037
0.6	0.221	0.163	0.043	0.38	0.229	0.172	0.02	0.023

Table 6
The effective bending stiffness tensors (12) and (17) for VPS plates with microstructure SR1.0. The results are shown normalized by the bending stiffness (13) of the underlying VPS matrix material.

f	$\frac{\widehat{M}_{1111}}{M_{1111}}$	$\frac{\widehat{M}_{2222}}{M_{2222}}$	$\frac{\widehat{M}_{1122}}{M_{1122}}$	$\frac{\widehat{M}_{1212}}{M_{1212}}$	$\frac{\widetilde{M}_{1111}}{M_{1111}}$	$\frac{\widetilde{M}_{2222}}{M_{2222}}$	$\frac{\widetilde{M}_{1122}}{M_{1122}}$	$\frac{\widetilde{M}_{1212}}{M_{1212}}$
0.05	0.856	0.856	0.763	0.939	0.84	0.84	0.758	0.851
0.1	0.74	0.74	0.588	0.881	0.718	0.718	0.578	0.703
0.15	0.643	0.643	0.454	0.824	0.622	0.622	0.443	0.562
0.2	0.563	0.563	0.355	0.77	0.545	0.545	0.341	0.438
0.25	0.496	0.496	0.279	0.719	0.482	0.482	0.262	0.333
0.3	0.437	0.437	0.219	0.668	0.427	0.427	0.2	0.247
0.35	0.383	0.383	0.17	0.617	0.38	0.38	0.152	0.18
0.4	0.338	0.338	0.134	0.569	0.338	0.338	0.113	0.128
0.45	0.297	0.297	0.104	0.523	0.3	0.3	0.082	0.09
0.5	0.259	0.259	0.079	0.473	0.265	0.265	0.057	0.061
0.55	0.224	0.224	0.06	0.425	0.232	0.232	0.037	0.04
0.6	0.193	0.193	0.045	0.38	0.202	0.202	0.021	0.026

Table 7
The effective bending stiffness tensors (12) and (17) for VPS plates with microstructure SR1.2. The results are shown normalized by the bending stiffness (13) of the underlying VPS matrix material.

f	$\frac{\widehat{M}_{1111}}{M_{1111}}$	$\frac{\widehat{M}_{2222}}{M_{2222}}$	$\frac{\widehat{M}_{1122}}{M_{1122}}$	$\frac{\widehat{M}_{1212}}{M_{1212}}$	$\frac{\widetilde{M}_{1111}}{M_{1111}}$	$\frac{\widetilde{M}_{2222}}{M_{2222}}$	$\frac{\widetilde{M}_{1122}}{M_{1122}}$	$\frac{\widetilde{M}_{1212}}{M_{1212}}$
0.05	0.847	0.86	0.76	0.938	0.829	0.849	0.756	0.85
0.1	0.724	0.75	0.584	0.88	0.7	0.733	0.576	0.701
0.15	0.625	0.66	0.453	0.825	0.6	0.641	0.44	0.56
0.2	0.541	0.584	0.353	0.772	0.519	0.568	0.338	0.435
0.25	0.467	0.518	0.275	0.718	0.451	0.508	0.259	0.328
0.3	0.405	0.464	0.216	0.669	0.394	0.457	0.197	0.241
0.35	0.35	0.415	0.168	0.62	0.343	0.413	0.148	0.173
0.4	0.299	0.372	0.13	0.571	0.298	0.373	0.109	0.12
0.45	0.254	0.334	0.101	0.523	0.256	0.338	0.078	0.081
0.5	0.213	0.3	0.076	0.477	0.218	0.306	0.054	0.052
0.55	0.175	0.268	0.056	0.428	0.182	0.276	0.034	0.031
0.6	0.141	0.239	0.041	0.383	0.148	0.247	0.018	0.018

Table 8
The effective bending stiffness tensors (12) and (17) for VPS plates with microstructure HE0.9. The results are shown normalized by the bending stiffness (13) of the underlying VPS matrix material.

f	$\frac{\widehat{M}_{1111}}{M_{1111}}$	$\frac{\widehat{M}_{2222}}{M_{2222}}$	$\frac{\widehat{M}_{1122}}{M_{1122}}$	$\frac{\widehat{M}_{1212}}{M_{1212}}$	$\frac{\widetilde{M}_{1111}}{M_{1111}}$	$\frac{\widetilde{M}_{2222}}{M_{2222}}$	$\frac{\widetilde{M}_{1122}}{M_{1122}}$	$\frac{\widetilde{M}_{1212}}{M_{1212}}$
0.05	0.869	0.861	0.774	0.941	0.86	0.848	0.805	0.896
0.1	0.762	0.749	0.603	0.885	0.746	0.723	0.654	0.805
0.15	0.674	0.656	0.472	0.829	0.65	0.621	0.538	0.724
0.2	0.599	0.576	0.366	0.775	0.569	0.534	0.448	0.649
0.25	0.533	0.506	0.284	0.717	0.498	0.46	0.378	0.581
0.3	0.476	0.447	0.22	0.665	0.436	0.394	0.323	0.516
0.35	0.425	0.395	0.166	0.613	0.379	0.336	0.28	0.455
0.4	0.378	0.347	0.124	0.561	0.328	0.284	0.247	0.395
0.45	0.338	0.304	0.092	0.527	0.281	0.237	0.221	0.337
0.5	0.296	0.262	0.063	0.457	0.238	0.196	0.2	0.281
0.55	0.261	0.226	0.041	0.406	0.198	0.158	0.182	0.227
0.6	0.226	0.19	0.025	0.353	0.163	0.126	0.163	0.179

Table 9
The effective bending stiffness tensors (12) and (17) for VPS plates with microstructure HE1.0. The results are shown normalized by the bending stiffness (13) of the underlying VPS matrix material.

f	$\frac{\widehat{M}_{1111}}{M_{1111}}$	$\frac{\widehat{M}_{2222}}{M_{2222}}$	$\frac{\widehat{M}_{1122}}{M_{1122}}$	$\frac{\widehat{M}_{1212}}{M_{1212}}$	$\frac{\widetilde{M}_{1111}}{M_{1111}}$	$\frac{\widetilde{M}_{2222}}{M_{2222}}$	$\frac{\widetilde{M}_{1122}}{M_{1122}}$	$\frac{\widetilde{M}_{1212}}{M_{1212}}$
0.05	0.866	0.866	0.776	0.942	0.855	0.855	0.806	0.897
0.1	0.756	0.756	0.603	0.885	0.735	0.735	0.655	0.805
0.15	0.662	0.662	0.465	0.826	0.637	0.637	0.538	0.722
0.2	0.588	0.588	0.367	0.774	0.554	0.554	0.447	0.645
0.25	0.521	0.521	0.286	0.719	0.482	0.482	0.374	0.574
0.3	0.461	0.461	0.224	0.674	0.419	0.419	0.317	0.506
0.35	0.419	0.419	0.172	0.612	0.363	0.363	0.272	0.44
0.4	0.363	0.363	0.127	0.564	0.312	0.312	0.237	0.376
0.45	0.319	0.319	0.093	0.514	0.266	0.266	0.209	0.315
0.5	0.28	0.28	0.065	0.46	0.224	0.224	0.186	0.256
0.55	0.242	0.242	0.044	0.411	0.186	0.186	0.168	0.201
0.6	0.209	0.209	0.029	0.359	0.152	0.152	0.15	0.153

Table 10
The effective bending stiffness tensors (12) and (17) for VPS plates with microstructure HE1.2. The results are shown normalized by the bending stiffness (13) of the underlying VPS matrix material.

f	$\frac{\widehat{M}_{1111}}{M_{1111}}$	$\frac{\widehat{M}_{2222}}{M_{2222}}$	$\frac{\widehat{M}_{1122}}{M_{1122}}$	$\frac{\widehat{M}_{1212}}{M_{1212}}$	$\frac{\widetilde{M}_{1111}}{M_{1111}}$	$\frac{\widetilde{M}_{2222}}{M_{2222}}$	$\frac{\widetilde{M}_{1122}}{M_{1122}}$	$\frac{\widetilde{M}_{1212}}{M_{1212}}$
0.05	0.855	0.87	0.77	0.942	0.84	0.866	0.804	0.896
0.1	0.742	0.767	0.602	0.885	0.713	0.755	0.65	0.802
0.15	0.65	0.681	0.465	0.833	0.609	0.662	0.531	0.716
0.2	0.567	0.605	0.366	0.775	0.523	0.584	0.437	0.634
0.25	0.497	0.541	0.285	0.722	0.45	0.516	0.362	0.557
0.3	0.434	0.484	0.221	0.669	0.387	0.457	0.301	0.481
0.35	0.379	0.434	0.167	0.62	0.331	0.404	0.252	0.408
0.4	0.328	0.387	0.128	0.568	0.281	0.356	0.213	0.336
0.45	0.283	0.346	0.094	0.515	0.237	0.312	0.181	0.268
0.5	0.239	0.307	0.066	0.466	0.197	0.271	0.155	0.203
0.55	0.201	0.273	0.047	0.417	0.16	0.233	0.133	0.145
0.6	0.161	0.24	0.03	0.366	0.127	0.198	0.114	0.096

Table 11
The effective bending stiffness tensors (12) and (17) for VPS plates with microstructure HR0.9. The results are shown normalized by the bending stiffness (13) of the underlying VPS matrix material.

f	$\frac{\widehat{M}_{1111}}{M_{1111}}$	$\frac{\widehat{M}_{2222}}{M_{2222}}$	$\frac{\widehat{M}_{1122}}{M_{1122}}$	$\frac{\widehat{M}_{1212}}{M_{1212}}$	$\frac{\widetilde{M}_{1111}}{M_{1111}}$	$\frac{\widetilde{M}_{2222}}{M_{2222}}$	$\frac{\widetilde{M}_{1122}}{M_{1122}}$	$\frac{\widetilde{M}_{1212}}{M_{1212}}$
0.05	0.855	0.846	0.764	0.937	0.844	0.834	0.765	0.864
0.1	0.745	0.73	0.577	0.876	0.719	0.704	0.589	0.749
0.15	0.653	0.634	0.444	0.816	0.616	0.601	0.458	0.649
0.2	0.573	0.547	0.343	0.758	0.527	0.517	0.359	0.559
0.25	0.508	0.478	0.264	0.701	0.448	0.447	0.282	0.478
0.3	0.447	0.412	0.193	0.64	0.377	0.387	0.221	0.402
0.35	0.398	0.358	0.151	0.587	0.311	0.334	0.174	0.33
0.4	0.348	0.304	0.111	0.526	0.249	0.287	0.136	0.261
0.45	0.306	0.256	0.075	0.468	0.191	0.243	0.105	0.198
0.5	0.267	0.212	0.056	0.413	0.137	0.203	0.078	0.142
0.55	0.228	0.169	0.038	0.353	0.088	0.165	0.055	0.092
0.6	0.192	0.13	0.022	0.301	0.05	0.128	0.036	0.055

Table 12
The effective bending stiffness tensors (12) and (17) for VPS plates with microstructure HR1.0. The results are shown normalized by the bending stiffness (13) of the underlying VPS matrix material.

f	$\frac{\widehat{M}_{1111}}{M_{1111}}$	$\frac{\widehat{M}_{2222}}{M_{2222}}$	$\frac{\widehat{M}_{1122}}{M_{1122}}$	$\frac{\widehat{M}_{1212}}{M_{1212}}$	$\frac{\widetilde{M}_{1111}}{M_{1111}}$	$\frac{\widetilde{M}_{2222}}{M_{2222}}$	$\frac{\widetilde{M}_{1122}}{M_{1122}}$	$\frac{\widetilde{M}_{1212}}{M_{1212}}$
0.05	0.856	0.855	0.762	0.938	0.838	0.841	0.765	0.864
0.1	0.742	0.742	0.588	0.879	0.71	0.715	0.589	0.748
0.15	0.643	0.641	0.448	0.815	0.603	0.615	0.457	0.645
0.2	0.562	0.56	0.348	0.759	0.513	0.534	0.356	0.553
0.25	0.497	0.491	0.267	0.703	0.434	0.466	0.277	0.467
0.3	0.436	0.429	0.204	0.645	0.364	0.408	0.215	0.388
0.35	0.385	0.374	0.155	0.592	0.3	0.357	0.165	0.312
0.4	0.338	0.324	0.112	0.534	0.242	0.312	0.126	0.244
0.45	0.295	0.277	0.086	0.482	0.189	0.27	0.095	0.183
0.5	0.256	0.234	0.063	0.427	0.141	0.232	0.069	0.132
0.55	0.221	0.197	0.045	0.377	0.1	0.196	0.049	0.091
0.6	0.189	0.159	0.031	0.321	0.065	0.162	0.033	0.059

Table 13
The effective bending stiffness tensors (12) and (17) for VPS plates with microstructure HR1.2. The results are shown normalized by the bending stiffness (13) of the underlying VPS matrix material.

f	$\frac{\widehat{M}_{1111}}{M_{1111}}$	$\frac{\widehat{M}_{2222}}{M_{2222}}$	$\frac{\widehat{M}_{1122}}{M_{1122}}$	$\frac{\widehat{M}_{1212}}{M_{1212}}$	$\frac{\widetilde{M}_{1111}}{M_{1111}}$	$\frac{\widetilde{M}_{2222}}{M_{2222}}$	$\frac{\widetilde{M}_{1122}}{M_{1122}}$	$\frac{\widetilde{M}_{1212}}{M_{1212}}$
0.05	0.847	0.862	0.759	0.938	0.827	0.85	0.763	0.863
0.1	0.728	0.751	0.584	0.879	0.69	0.731	0.585	0.744
0.15	0.627	0.659	0.45	0.82	0.58	0.636	0.451	0.637
0.2	0.544	0.581	0.342	0.76	0.487	0.558	0.347	0.537
0.25	0.473	0.513	0.267	0.705	0.408	0.494	0.266	0.445
0.3	0.408	0.451	0.206	0.65	0.339	0.439	0.201	0.357
0.35	0.357	0.399	0.155	0.595	0.28	0.392	0.151	0.279
0.4	0.308	0.353	0.115	0.544	0.228	0.349	0.111	0.209
0.45	0.266	0.311	0.091	0.497	0.183	0.311	0.08	0.151
0.5	0.229	0.275	0.069	0.45	0.144	0.276	0.055	0.105
0.55	0.195	0.24	0.052	0.402	0.11	0.244	0.037	0.07
0.6	0.163	0.206	0.037	0.353	0.083	0.213	0.023	0.045

References

Anon., 2019. MATLAB R2019A Version Documentation. Mathworks, Natick, Massachusetts, USA.

Argyris, J.H., Isaac, F., Dieter, W.S., 1968. The TUBA family of plate elements for the matrix displacement method. Aeronaut. J. 72, 701–709.

Arnold, D.N., Madureira, A.L., S. Zhang, S., 2002. On the range of applicability of the Reissner–Mindlin and Kirchhoff–Love plate bending models. J. Elasticity 67, 171–185.

Bell, K., 1969. A refined triangular plate bending finite element. Internat. J. Numer. Methods Engrg. 1, 101–122.

Caillerie, D., 1984. Thin elastic and periodic plates. Math. Methods Appl. Sci. 6, 159–191.

Ciarlet, P.G., Destuynder, P., 1979. A justification of the two-dimensional linear plate model. J. Mec. 18, 315–344.

Destuynder, P., Nevers, T., 1988. Une modification du modèle de Mindlin pour les plaques minces en flexion présentant un bord libre. Model. Math. Anal. Numer. 22, 217–242.

Duvaut, G., Metellus, A.M., 1976. Homogénéisation d'une plaque mince en flexion de structure périodique et symétrie. C. R. Acad. Sci., Paris A 283, 947–950.

Guttag, M., Karimi, H.H., Falcón, C., Reis, P.M., 2018. Aeroelastic deformation of a perforated strip. Phys. Rev. Fluids 3, 014003.

Kohn, R.V., Vogelius, M., 1984. A new model for thin plates with rapidly varying thickness. Int. J. Solids Struct. 20, 333–350.

Love, A.E.H., 1888. The small free vibrations and deformation of a thin elastic shell. Phil. Trans. R. Soc. A 179, 491–546.

Morley, L.S.D., 1968. The triangular equilibrium element in the solution of plate bending problems. Aeronaut. Q. 19, 149–169.

Pezzulla, M., Strong, E.F., Gallaire, F., Reis, P.M., 2020. Deformation of porous flexible strip in low and moderate Reynolds number flows. Phys. Rev. Fluids 5, 084103.

Reddy, J.N., 2007. Theory and Analysis of Elastic Plates and Shells. CRC Press, Boca Raton.

Sab, K., Lebée, A., 2015. Homogenization of Heterogeneous Thin and Thick Plates. John Wiley & Sons.

Shrimali, B., Lefèvre, V., Lopez-Pamies, O., 2019. A simple explicit homogenization solution for the macroscopic elastic response of isotropic porous elastomers. J. Mech. Phys. Solids 122, 364–380.

Shrimali, B., Lopez-Pamies, O., 2021. https://github.com/bhaveshshrimali/PlatesHomogenization.

Shrimali, B., Parnell, W.J., Lopez-Pamies, O., 2020. A simple explicit model constructed from a homogenization solution for the large-strain mechanical response of elastomeric syntactic foams. Int. J. Non-Linear Mech. 126, 103548.

Spinelli, S.A., Lefèvre, V., Lopez-Pamies, O., 2015. Dielectric elastomer composites: A general closed-form solution in the small-deformation limit. J. Mech. Phys. Solids 83, 263–284.

Timoshenko, S.P., Woinowsky-Krieger, S., 1959. Theory of Plates and Shells. McGraw-Hill, New York.

Veiga, L.B.D., Niiranen, J., Stenberg, R., 2007. A family of C^0 finite elements for Kirchhoff plates I: Error analysis. SIAM J. Numer. Anal. 19, 149–168.